



Light Curves of Hydrogen-poor Superluminous Supernovae from the Palomar Transient Factory

Annalisa De Cia^{1,2,21}, A. Gal-Yam¹, A. Rubin¹, G. Leloudas^{1,3}, P. Vreeswijk¹, D. A. Perley⁴, R. Quimby^{5,6}, Lin Yan^{7,8}, M. Sullivan⁹, A. Flörs², J. Sollerman¹⁰, D. Bersier⁴, S. B. Cenko^{11,12}, M. Gal-Yam¹³, K. Maguire¹⁴, E. O. Ofek¹, S. Prentice⁴, S. Schulze¹, J. Spyromilio², S. Valenti¹⁵, I. Arcavi^{16,17,22}, A. Corsi¹⁸, D. A. Howell^{16,17}, P. Mazzali^{1,4,19}, M. M. Kasliwal²⁰, F. Taddia¹⁰, and O. Yaron¹

¹ Department of Particle Physics and Astrophysics, Weizmann Institute of Science, Rehovot 76100, Israel

² European Southern Observatory, Karl-Schwarzschild Str. 2, D-85748 Garching bei München, Germany; aedcia@eso.org

³ Dark Cosmology Centre, Niels Bohr Institute, University of Copenhagen, Juliane Maries Vej 30, DK-2100, Copenhagen, Denmark

⁴ Astrophysics Research Institute, Liverpool John Moores University, Liverpool Science Park, 146 Brownlow Hill, Liverpool L35RF, UK

⁵ Department of Astronomy, San Diego State University, San Diego, CA 92182, USA

⁶ Kavli IPMU (WPI), UTIAS, The University of Tokyo, Kashiwa, Chiba 277-8583, Japan

⁷ MS100-22, Caltech/IPAC, California Institute of Technology, Pasadena, CA 91125, USA

⁸ Caltech Optical Observatories, California Institute of Technology, Pasadena, CA 91125, USA

⁹ Department of Physics and Astronomy, University of Southampton, Southampton SO17 1BJ, UK

¹⁰ The Oskar Klein Centre, Department of Astronomy, Stockholm University, AlbaNova, SE-10691, Stockholm, Sweden

¹¹ Astrophysics Science Division, NASA Goddard Space Flight Center, Mail Code 661, Greenbelt, MD 20771, USA

¹² Joint Space-Science Institute, University of Maryland, College Park, MD 20742, USA

¹³ The Schwartz/Reisman Science Education Center, Weizmann Institute of Science, Rehovot, Israel

¹⁴ Astrophysics Research Centre, School of Mathematics and Physics, Queen's University Belfast, Belfast BT7 1NN, UK

¹⁵ Department of Physics, University of California, Davis, CA 95616, USA

¹⁶ Las Cumbres Observatory, 6740 Cortona Dr. Suite 102, Goleta, CA 93117, USA

¹⁷ Department of Physics, University of California, Santa Barbara, CA 93106-9530, USA

¹⁸ Department of Physics and Astronomy, Texas Tech University, Box 1051, Lubbock, TX 79409-1051, USA

¹⁹ Max-Planck-Institut für Astrophysik, Karl-Schwarzschild-Str. 1, D-85748 Garching, Germany

²⁰ Astronomy Department, California Institute of Technology, Pasadena, CA 91125, USA

Received 2017 August 4; revised 2018 March 22; accepted 2018 March 23; published 2018 June 15

Abstract

We investigate the light-curve properties of a sample of 26 spectroscopically confirmed hydrogen-poor superluminous supernovae (SLSNe-I) in the Palomar Transient Factory survey. These events are brighter than SNe Ib/c and SNe Ic-BL, on average, by about 4 and 2 mag, respectively. The peak absolute magnitudes of SLSNe-I in rest-frame g band span $-22 \lesssim M_g \lesssim -20$ mag, and these peaks are not powered by radioactive ^{56}Ni , unless strong asymmetries are at play. The rise timescales are longer for SLSNe than for normal SNe Ib/c, by roughly 10 days, for events with similar decay times. Thus, SLSNe-I can be considered as a separate population based on photometric properties. After peak, SLSNe-I decay with a wide range of slopes, with no obvious gap between rapidly declining and slowly declining events. The latter events show more irregularities (bumps) in the light curves at all times. At late times, the SLSN-I light curves slow down and cluster around the ^{56}Co radioactive decay rate. Powering the late-time light curves with radioactive decay would require between 1 and $10 M_{\odot}$ of Ni masses. Alternatively, a simple magnetar model can reasonably fit the majority of SLSNe-I light curves, with four exceptions, and can mimic the radioactive decay of ^{56}Co , up to ~ 400 days from explosion. The resulting spin values do not correlate with the host-galaxy metallicities. Finally, the analysis of our sample cannot strengthen the case for using SLSNe-I for cosmology.

Key words: supernovae: general

Supporting material: figure sets, machine-readable tables

1. Introduction

Since the advent of wide-field untargeted transient surveys, a class of superluminous supernovae (SLSNe) that are over 10 times more luminous than regular SNe (see Gal-Yam 2012 for a review), with absolute magnitudes $\lesssim -21$ mag, has emerged. The first few objects showed a striking diversity, e.g., SN 2005ap (Quimby et al. 2007), SN 2006gy (Ofek et al. 2007; Smith et al. 2007), and SN 2007bi (Gal-Yam et al. 2009), leading to a natural division between H-rich events (SLSNe-II) and H-poor events (SLSNe-I). Most SLSNe-II show narrow lines (SLSN-IIIn) and are powered by the

interaction of the SN ejecta with the circumstellar medium (CSM; e.g., Chevalier & Fransson 1994; Chugai & Danziger 1994; Chevalier & Irwin 2011; Ofek et al. 2013; Inserra et al. 2018). SLSNe-I are less well-understood, and the physical processes that dominate these explosions are still under debate.

Quimby et al. (2011) inspected the first sample of SLSNe-I, and found that they have UV-bright light curves over extended periods of time. Quimby et al. (2011) also showed similarity in their spectral features and suggested that their progenitors may have initial masses $90 < M < 130 M_{\odot}$, perhaps exploding as core-collapse SNe with massive ejecta interacting with a H-poor CSM. Asymmetry in the ejecta can hide signatures of hydrogen or helium in SLSN-I spectra (Kozyreva & Blinnikov 2015), as well as ionization (Mazzali

²¹ ESO fellow.

²² Einstein Fellow.

et al. 2016). Gal-Yam (2012) proposed that a group of slowly declining events (SLSNe-R), similar to SN 2007bi, have late-time light curves that are powered by radioactivity and could be associated with pair-instability SNe (PISNe; Barkat et al. 1967; Heger & Woosley 2002; Gal-Yam et al. 2009), but this is widely debated (Dessart et al. 2012; Nicholl et al. 2013). Inserra et al. (2013) showed that the late-time decay of a few SLSNe slows down to a “tail” that could be explained if the light curves were powered by the spin-down of a newly born magnetar (Kasen & Bildsten 2010). Nicholl et al. (2015a) studied a sample of SLSNe and suggested that the ejecta mass is the main driver of the observed diversity. More recently, Nicholl et al. (2017) fitted a magnetar model to the literature sample of SLSNe-I.

Early-time bumps (pre-peak or double peaks, or excess emission) have been observed in some SLSNe light curves, such as SN 2006oz (Leloudas et al. 2012), LSQ 14bdq (Nicholl et al. 2015b), PTF 12dam and iPTF 13dcc (Vreeswijk et al. 2017), and DES 14X3taz (Smith et al. 2016). These early bumps can be explained by shock-cooling or CSM interaction models (e.g., Nakar & Sari 2010; Rabinak & Waxman 2011; Chatzopoulos et al. 2012; Piro 2015). Such early bumps or double-peaked light curves may in fact be common among SLSNe (Nicholl & Smartt 2016). Late-time bumps (postpeak) have also been observed in a few cases, such as for SN 2007bi (Gal-Yam et al. 2009), iPTF 13ehe (Yan et al. 2015), PS1-14bj (Lunnan et al. 2016), and SN 2015bn (Nicholl et al. 2016). Wiggles in the late-time decay have often been observed in a handful of slowly declining SLSNe by Inserra et al. (2017). Such late-time bumps cannot be explained by magnetar and radioactive decay models. Late-time emergence of hydrogen emission has been detected in a few cases (e.g., iPTF 15esb; Yan et al. 2015, 2017), and in these cases it was explained with substantial mass loss that occurred shortly before the progenitors of the SLSNe exploded (Yan et al. 2015, 2017). Indeed, Liu et al. (2017) showed that the light curves of iPTF 15esb could be explained with a multiple-shell CSM interaction model. The diversity observed so far in H-poor SLSNe seems to indicate that multiple processes may contribute to powering their light curves.

In this paper, we present a sample of 26 SLSNe-I from the Palomar Transient Factory (PTF; Law et al. 2009; Rau et al. 2009) and its successor the intermediate Palomar Transient Factory (iPTF). This is the largest sample of SLSNe-I homogeneously selected from a single survey available so far. Here we characterize and discuss the properties of the light curves of these events, and compare them to a large PTF sample of SNe Ib/c and Ic-BL (with broad lines). We address the question on how luminous SLSNe-I are, and whether they can be considered a separate population based on their light-curve properties. We investigate whether SLSNe-R are a separate class of events, and whether we can use SLSNe-I for cosmology. The spectra of (i)PTF SLSNe, and the host galaxies of PTF SLSNe up to 2012 are studied in Quimby et al. (2018) and Perley et al. (2016), respectively.

The paper is organized as follows. In Sections 2 and 3, we describe the SLSN sample and observations, respectively. We characterize the SN light curves in Section 4, discuss our results in Section 5, and present our conclusions in Section 6. We adopt the cosmological parameters $H_0 = 70 \text{ km s}^{-1} \text{ Mpc}^{-1}$, $\Omega_m = 0.3$, and $\Omega_\Lambda = 0.7$ throughout the paper.

Table 1
The PTF Sample of 26 Hydrogen-poor SLSNe

PTF ID	R.A. (hh:mm:ss)	Decl. (°:′:″)	z	Type	A_V^{a} (mag)
09as	12:59:15.78	+27:16:38.5	0.1864	I	0.02
09atu	16:30:24.55	+23:38:25.0	0.5014	I	0.13
09cnd	16:12:08.94	+51:29:16.2	0.2585	I	0.06
09cwl	14:49:10.08	+29:25:11.4	0.3502	I	0.04
10aagc	09:39:56.93	+21:43:16.9	0.2067	I	0.07
10bfz	12:54:41.27	+15:24:17.0	0.1699	I	0.05
10bjp	10:06:34.30	+67:59:19.0	0.3585	I	0.17
10cwr	11:25:46.67	-08:49:41.2	0.2301	I	0.10
10hgi	16:37:47.04	+06:12:32.3	0.0982	I	0.22
10nmn	15:50:02.79	-07:24:42.1	0.1236	I/R	0.42
10uhf	16:52:46.68	+47:36:22.0	0.2879	I	0.05
10vqv	03:03:06.84	-01:32:34.9	0.4520	I	0.17
10vwg	18:59:32.86	+19:24:25.7	0.1901	I/R	1.41
11dij	13:50:57.77	+26:16:42.8	0.1429	I	0.03
11hrq	00:51:47.22	-26:25:10.0	0.0571	I/R	0.04
11rks	01:39:45.51	+29:55:27.0	0.1924	I	0.11
12dam	14:24:46.20	+46:13:48.3	0.1075	I/R	0.03
12gtv	16:01:15.23	+21:23:17.4	0.1768	I	0.18
12hni	22:31:55.86	-06:47:49.0	0.1056	I	0.16
12mxx	22:30:16.68	+27:58:21.9	0.3274	I	0.12
13ajg	16:39:03.95	+37:01:38.4	0.7403	I	0.04
13bdd	12:36:56.14	+13:07:45.5	0.4030	I	0.13
13bjz	10:38:19.83	+24:24:51.0	0.2712	I	0.06
13cjq	00:14:27.18	+24:17:08.8	0.3962	I	0.13
13dcc	02:57:02.50	-00:18:44.0	0.4308	I/R	0.18
13ehe	06:53:21.50	+67:07:56.0	0.3434	I/R	0.14

Note.

^a Galactic foreground extinction.

2. The PTF Sample of SLSNe

PTF was a wide-field (7.26 deg^2 field of view), nontargeted survey designed to investigate the optical transient and variable sky (Law et al. 2009; Rau et al. 2009), carried out using the refurbished CFH12k camera (Rahmer et al. 2008), mounted on the Palomar Observatory 48-inch Samuel Oschin Telescope (P48), in California. The PTF survey is optimized for the discovery of SNe of different types. Since its start in 2009, PTF has discovered and classified over 3000 SNe. The classification and follow-up observations of these SNe are performed through a wide network of telescopes (Gal-Yam et al. 2011), as described below for our sample. The selection of SN candidates for spectroscopic classification within the PTF survey is not free of biases. For example, SLSN searches may have given more weight to candidates that were brighter than their host galaxies. Nevertheless, PTF has discovered a large number of SLSNe-II as well, which can explode in normal host galaxies (e.g., Perley et al. 2016), reassuring us that such selection biases are not dominant.

The 26 SLSNe discussed in this paper are all the hydrogen-poor SLSNe discovered between 2009 and 2013 by the (i)PTF survey. The sample is shown in Table 1. This significantly increases the sample of about 50 currently known H-poor SLSNe with reported spectral classification in the literature (either published or with spectra reported in Astronomer’s Telegrams; e.g., Nicholl et al. 2015a; Lunnan et al. 2018; Schulze et al. 2018), 10 of which have been discovered by PTF and are part of this work as well.

The PTF SLSNe in our sample have been spectroscopically classified as SLSNe-I by Quimby et al. (2018). This sample is thus spectroscopically selected and assumes no luminosity thresholds. The sample of PTF SLSN host galaxies of Perley et al. (2016) is slightly different because that work also applied a luminosity cut, while PTF 12hni and PTF 12gty are presented here for the first time. PTF 12hni is classified as an SLSN-I by Quimby et al. (2018) with some uncertainty, and having possible matches to SN Ia and SN Ic. In addition, three other events are reported as possible SLSNe by Quimby et al. (2018), namely PTF 09q, PTF 10gzb, and PTF 11mnb, but are most likely not SLSNe, and therefore we do not include these in our sample.²³

What makes the PTF sample unique is not only the fact that it is homogeneously selected from a single survey, but also that its average redshift is low ($\langle z \rangle = 0.27$; see Section 2.1). A higher- z ($0.3 < z < 1.6$) sample of 17 SLSNe-I from the Pan-STARRS1 Medium Deep Survey (PS1; Kaiser et al. 2010) is presented by Lunnan et al. (2018). In addition, the light-curve coverage of the PTF sample often extends to late times, beyond 100 days after the peak for half of the sample. The currently known H-poor SLSNe in the literature typically lack photometry later than 120 days after peak (e.g., Nicholl et al. 2015a). Jerkstrand et al. (2017) and Inserra et al. (2017) have studied a small sample of slow-evolving SLSNe, with data coverage up to 400 days after peak.

As a comparison sample, we also select all Type Ib, Ib/c, Ic, and Ic-BL SNe discovered between 2009 and 2013 by PTF. These SNe are studied in more detail in Arcavi et al. (2010), Corsi et al. (2016), Prentice et al. (2016), and Taddia et al. (2018b), and will be presented in full in forthcoming publications (C. Barbarino et al. 2018, in preparation; C. Fremling et al. 2018, in preparation; E. Karamehmetoglu et al. 2018, in preparation; and S. Schulze et al. 2018, in preparation).

We derive the rest-frame g -band absolute magnitudes, M_g , from the apparent r magnitudes m_r including the k -correction term K_{gr} described in Section 3.12 and listed in Table 9 ($M_g = m_r - DM(z) - K_{gr}$, where $DM(z)$ is the distance modulus for a given redshift z , and m_r is corrected for foreground Galactic extinction, reported in Table 1). Figure 1 shows the rest-frame M_g light curves of all 26 SLSNe in our sample.

2.1. The Redshift Distribution

Although most normal SNe are observed in the nearby universe ($z \lesssim 0.2$), the most luminous ones can be detected out to higher redshift. SNe Type Ia, for instance, are currently discovered out to $z \sim 2$ in deep imaging (Jones et al. 2013). A few SLSNe have been studied out to $z \sim 4$ in the deepest surveys (Cooke et al. 2012), although in limited detail compared to nearby targets. Recently, a small sample of $z \sim 2$ SLSNe has been studied by Moriya et al. (2018) and Curtin et al. (2018). In the future, the *James Webb Space Telescope* is expected to be able to detect SLSNe out to $z \sim 20$ (Abbott et al. 2017). The PTF survey typically discovers SLSNe below $z \lesssim 1$.

²³ For PTF 09q, there is a single spectrum available, which is well consistent with an SN Ic, and its host galaxy is a massive galaxy (Quimby et al. 2018). Three spectra are available for PTF 10gzb, but one is mostly featureless and lacks the typical SLSN O II features, and the other two are well-matched with an SN Ic-BL (Quimby et al. 2018). PTF 11mnb is most likely an SN Ic, as studied in detail by Taddia et al. (2018a).

The redshifts in our SLSN sample are all measured spectroscopically and normally measured from narrow Mg II absorption lines in the SN spectra. The typical uncertainties on the redshift estimates are of the order of 0.0005, given the typical resolution of the follow-up spectra (described in Quimby et al. 2018). The redshifts in Table 1 are taken from Quimby et al. (2018) for all events up to 2012, except for PTF 10vvg, for which we adopt the slightly more accurate redshift of Perley et al. (2016). We adopt the redshifts of Vreeswijk et al. (2014) for PTF 13ajg and of Yan et al. (2015) for PTF 13ehe. For the other 2013 events, we directly measure the redshifts from the Mg II narrow absorption lines in the spectra. In PTF 13ehe, the most common spectral features are very weak. The redshift measurement is based on a weak O III 5007 emission line, and its uncertainty is of the order of 0.001.

Figure 2 shows the redshift distribution of our sample, where the mean redshift is $\langle z \rangle = 0.27$ with standard deviation $\sigma_z = 0.15$. The volume-weighted mean is $\langle z \rangle = 0.33$.²⁴

The mean redshift of the PTF H-poor SLSN sample presented here is comparable to the “golden” SLSN sample of Nicholl et al. (2015a; $\langle z \rangle = 0.22$, while $\langle z \rangle = 0.63$ for their “silver” sample), and the SLSN host sample of Leloudas et al. (2015; $\langle z \rangle = 0.34$ with a standard deviation of 0.2). On the other hand, SLSNe discovered by PS1 tend to be at higher redshifts, typically $z > 0.5$ (McCrumb et al. 2015), and in particular $0.3 < z < 1.6$ (Lunnan et al. 2018).

The drop of the redshift distribution above $z \sim 0.5$ in our sample is an observational selection effect due to the limiting magnitude of the PTF survey ($m_{r,\text{lim}} \sim 20.5$ mag; Cao et al. 2016). This limit hampers further investigations of the evolution of the sample properties with redshift.

3. Observations and Data Processing

3.1. Palomar P48 Discovery and Imaging

As part of standard PTF operations, SN candidates are discovered in P48 images using image subtraction in Mould-R (r) or the Sloan Digital Sky Survey (SDSS; York et al. 2000; SDSS Collaboration et al. 2017) g' filter. The best SN candidates are then classified spectroscopically and followed-up with other telescopes. The raw P48 images are initially processed by the Infrared Processing and Analysis Center (IPAC; Laher et al. 2014). The photometric calibration and system are described in Ofek et al. (2012). Image-subtraction point-spread function (PSF) photometry is performed with a custom routine (a pipeline written by one of us (M.S.) and used extensively in PTF; e.g., Sullivan et al. 2006; Ofek et al. 2014a; Firth et al. 2015; Dimitriadis et al. 2017). This pipeline constructs deep reference images—either before the SN explosion or after the SN has faded—and astrometrically aligns the images using the Automated Astrometry described in Hogg et al. (2008) and the Naval Observatory Merged Astrometric Dataset (NOMAD; Zacharias et al. 2004). The image PSFs are then matched in order to perform the image subtraction and then to extract the PSF photometry of the SN only (where the contribution of the reference image has been subtracted). The fluxes are calibrated against SDSS Data Release 10 (Ahn et al. 2014) when available, otherwise against

²⁴ A Gaussian fit through the redshift distribution data prefers a mean redshift $\langle z \rangle = 0.16$ with a standard deviation $\sigma_z = 0.20$ for a z bin size of 0.05. The mean $\langle z \rangle$ is 0.11 and 0.17 for bin sizes of 0.01 and 0.1, respectively.

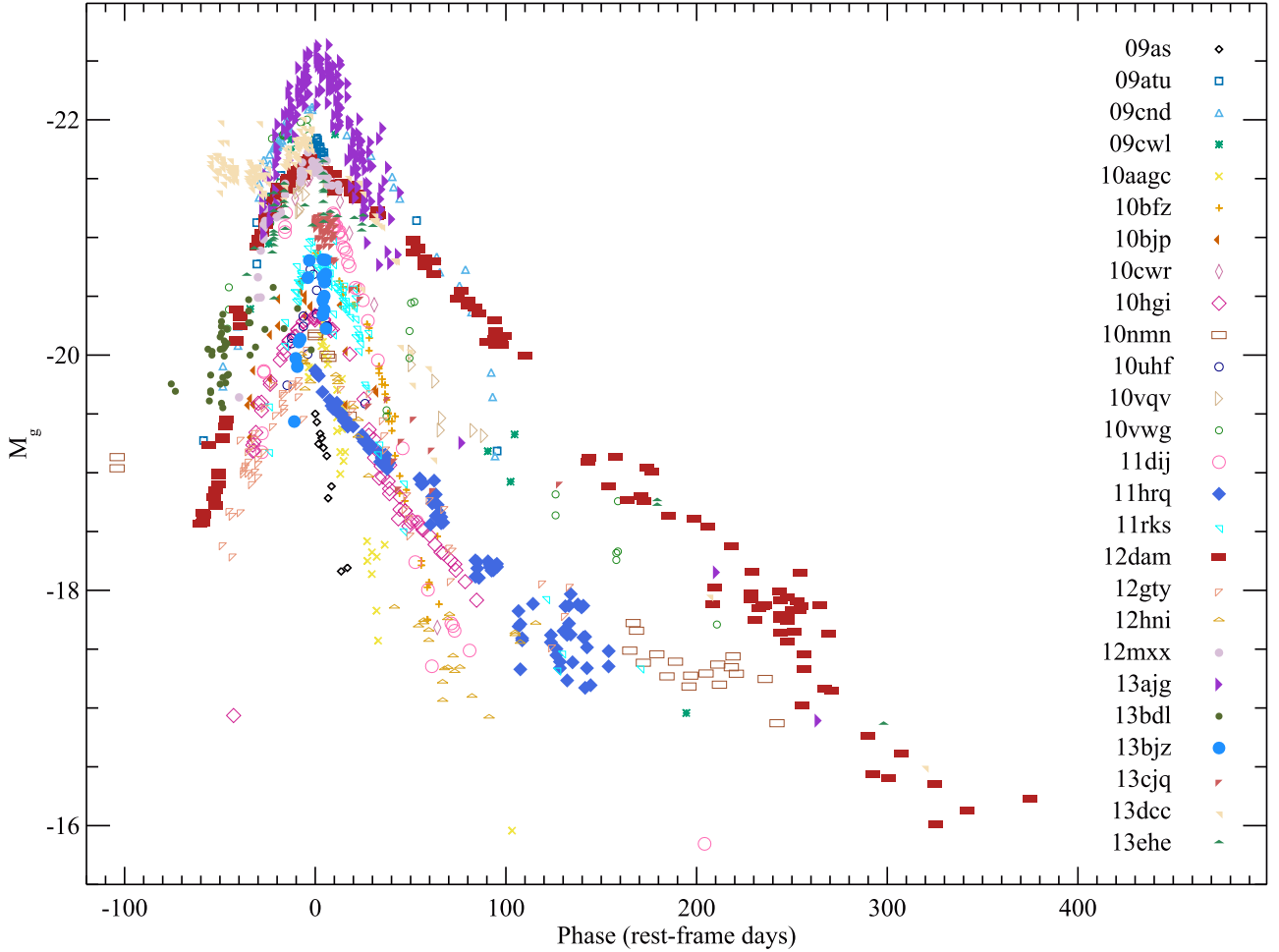


Figure 1. Rest-frame M_g light curves of the 26 H-poor SLSNe in our sample. The error bars are omitted here for readability, but are shown in Figures 18(a)–(e).

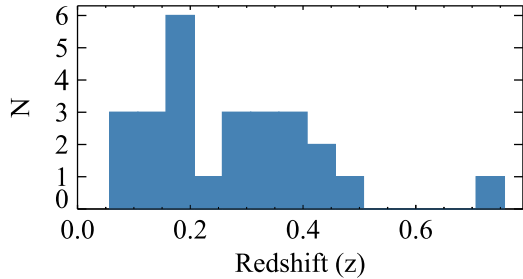


Figure 2. Redshift distribution of the sample of hydrogen-poor SLSNe presented in Table 1.

the photometric catalog of Ofek et al. (2012), and making no assumption on the SLSN colors.

The formal uncertainties derived with the MS pipeline only include statistical uncertainties, but not uncertainties from poor image subtraction or calibration. As a result, the formal uncertainties are slightly underestimated. For example, under excellent data coverage, we can observe a larger scatter than that accounted for by the formal uncertainties. The best example is for iPTF 13ajg, which shows a scatter of ~ 0.5 mag around peak. We quantify the additional source of uncertainty by assuming $\chi^2_\nu = 1$ for the light-curve fit around the peak of iPTF 13ajg (see Section 4.1). The additional required uncertainty is 0.05 mag, which we add to all formal errors derived

with the MS pipeline (i.e., for the data taken with the P48, P60, and LT telescopes; see below), to account for poor image subtraction or calibration.

Nondetections, and in particular the last nondetection limits before the SN discoveries, are not included in our analysis. The reason for this is that nondetections are largely dominated by noisy data and are uninformative. In addition, in most cases the SLSNe-I were discovered long after explosions. For the case of PTF 12dam, co-adds of the prediscivery nondetections are presented in Vreeswijk et al. (2017). The analysis presented in this paper is independent of the nondetection limits. Thus, we leave the treatment of prediscivery limits, which is beyond the scope of this paper, for future case-by-case studies.

3.2. Palomar P60 Imaging

Follow-up imaging was obtained with the Palomar 60-inch telescope (P60; Cenko et al. 2006). The filters employed for our observations are Johnson B (Bessell 1990), Kron R (similar to Cousins R_C , Bessell 1990), Sloan i' and z' (Fukugita et al. 1996), and Gunn g (Thuan & Gunn 1976). The SN photometry is extracted with the same routine described above for the P48 data processing, but calibrated using the AAVSO Photometric All-Sky Survey (APASS; Henden et al. 2009) for the B filter or for fields that are not covered by the SDSS footprint.

3.3. Keck/LRIS Imaging

We observed PTF SLSNe at late times using the Low-Resolution Imaging Spectrometer (LRIS) on the Keck I telescope to monitor the late-time evolution of the light curve or to produce a deep reference image (after the SN has faded) for image subtraction or host galaxy study (Perley et al. 2016). Images were processed using standard techniques via the custom pipeline LPIPE²⁵ and co-added using SWarp. Photometry was performed after image subtraction of the reference image (taken from Perley et al. 2016), with the custom-made IRAF routine `mkdifflc` (Gal-Yam et al. 2004, 2008).

3.4. Liverpool Telescope Imaging

Follow-up imaging was also obtained with the 2 m robotic Liverpool Telescope (LT, Steele et al. 2004) at the Roque de los Muchachos Observatory on La Palma, Spain, with the RATCAM and IO:O optical imagers in g , r , and i filters (similar to SDSS). The images were processed following Maguire et al. (2014) and using the image-subtraction PSF photometry custom routine described above for the P48 Telescope.

3.5. Las Cumbres Observatory Imaging

The LCO (previously known as LCOGT; Brown et al. 2013) data have been reduced using a custom pipeline (Valenti et al. 2016). The pipeline employs standard procedures (PYRAF, DAOPHOT) in a Python framework. Host galaxy flux was removed using image subtraction technique (High Order Transform of PSF ANd Template Subtraction, HOTPANTS²⁶). PSF magnitudes were computed on the subtracted images and transformed to the standard SDSS filter system (for gri) via standard star observations taken during clear nights.

3.6. Discovery Channel Telescope Imaging

We imaged several of the SLSNe in our sample with the Large Monolithic Imager (LMI) mounted on the 4.3 m Discovery Channel Telescope (DCT) in Happy Jack, AZ. The LMI images were processed using a custom IRAF pipeline for basic detrending (bias subtraction and flat fielding), and individual dithered images were combined using SWarp (Bertin et al. 2002). SN magnitudes were measured using aperture photometry with the inclusion radius matched to the FWHM of the image PSF. Photometric calibration was performed relative to point sources from the SDSS (York et al. 2000; SDSS Collaboration et al. 2017).

No DCT reference images are available for image subtraction, so we account for the contribution of the host galaxies by subtracting the host magnitudes from the observed fluxes, and we include this into the photometric uncertainty budget. The SLSNe iPTF 13dcc and 13ehe were observed with the DCT. The host galaxy of iPTF 13dcc has $B = 26.3 \pm 0.2$ and $i = 25.0 \pm 0.2$ (D. Perley et al. 2018, in preparation), and we assume $g = 26.3 \pm 0.2$ and $r = 25.0 \pm 0.2$ for the subtraction of the host galaxy contribution to the r -band data point, which is a reasonable assumption given typical host galaxy colors (Perley et al. 2016). The host galaxy of iPTF 13ehe has

$B = 25.0 \pm 0.1$ and $R = 24.0 \pm 0.1$. (D. Perley et al. 2018, in preparation), which we use to subtract the host-galaxy contribution. For both SLSNe, this host-galaxy correction affects significantly (by 0.2 mag) only the last r -band epoch of their light curves. In both cases, the DCT data points are consistent with the photometry from other facilities, including late-time *Hubble Space Telescope (HST)* photometry (Section 3.9).

3.7. Swift/UVOT Imaging

A number of supernovae in our sample were observed with the UltraViolet/Optical Telescope (UVOT; Roming et al. 2005) on board the *Swift* Gamma-Ray Burst Explorer (Gehrels et al. 2004). Data were processed using the standard UVOT pipeline, and photometry was extracted at the supernova location using a 3'' radius. Photometric calibration was calculated using the zero point measurements from Poole et al. (2008) and Breeveld et al. (2010). The magnitudes reported in Tables 11 and 12 are all on the AB system. No attempt has been made to correct for underlying contributions from the host galaxy emission. At these redshifts, the host galaxy contribution should not significantly affect the observed UV flux in most cases. This may not be true for some cases, in particular for PTF 12dam and its luminous underlying starburst host galaxy (Chen et al. 2015; Thöne et al. 2015; Perley et al. 2016; Cikota et al. 2017). However, even in this case, the host galaxy brightness in the $F225W$ filter is 19.94 ± 0.17 (Perley et al. 2016), which is 1–2 mag fainter than the unsubtracted SN photometry (Nicholl et al. 2013; Chen et al. 2015).

3.8. Palomar P200/Large Format Camera (LFC) Imaging

Follow-up imaging was obtained with the Palomar 200-inch Hale Telescope with the LFC.²⁷ The data reduction was performed with standard IRAF tasks. The SN magnitudes were derived by extracting aperture photometry at different radii, for the SN images and the reference image, and subtracting the host contribution. For the case of PTF 09cnd, we measure the photometry using both the image-subtraction routine `mkdifflc` and aperture photometry, and take the average between the two results. For the case of PTF 10cwr, no reference image is available, so we extract aperture photometry with a 3'' radius and subtract the host magnitude reported by Perley et al. (2016) and include this into the photometric uncertainty budget.

3.9. HST

The SLSNe iPTF 13dcc and iPTF 13ehe were observed with the Advanced Camera for Surveys in the Wide Field Channel on board the *HST* with the $F625W$ filter, as part of the GO-13858 program (PI A. De Cia). The data were reduced using the CALACS software, which contains corrections for degradation of the charge transfer efficiency and electronic artifacts (bias-shift and -striping effects). Cosmic rays were removed using the LA Cosmic routine (van Dokkum 2001). The images were then processed with DrizzlePac 2.0,²⁸ with inverse variance map (IVM) weighting and assuming a pixel scale of 0''.033 and a pixel fraction of 0.6.

²⁵ <http://www.astro.caltech.edu/~dperley/programs/lpipe.html>

²⁶ <http://www.astro.washington.edu/users/becker/v2.0/hotpants.html>

²⁷ <http://www.astro.caltech.edu/palomar/about/telescopes/hale.html>

²⁸ <http://drizzlepac.stsci.edu>

The SN PSF is resolved from the more extended host galaxies. For iPTF 13dcc, the PSF of the host has an FWHM of 3.2 pixels ($0.^{\circ}11$), while field stars have 2.4 pixels ($0.^{\circ}08$). iPTF 13ehe is separated from its host galaxy. The SN PSFs were fitted and thus isolated from their host galaxies using a custom IDL routine. The PSF SN photometry was then extracted assuming *HST* zeropoints and applying a correction for an aperture of $0.^{\prime\prime}5$ radius.

3.10. Literature Data Collection

We complement the photometric data set of the SLSNe in our sample with the data published in Quimby et al. (2011), Pastorello et al. (2010), Inserra et al. (2013), Nicholl et al. (2013), Chen et al. (2015), and Vreeswijk et al. (2014). The literature photometry is showed in Figures 18(a)–(e). The purpose of including the literature data in this paper is to collect the most complete available light curves for the SLSNe in our sample. The r -band photometry is used to calculate the rest-frame g -band photometry, which is reported in Table 12. Because the sources of our observations are already diverse, the inclusion of literature data does not affect significantly the quality of our data set.

The full light curve of PTF 10nnm will be presented by O. Yaron et al. (2018, in preparation), including a wider coverage of the SN peak, which is not presented in this paper.

We exclude from the analysis a couple of published photometry data points in cases of disagreement with the photometry secured with other (multiple) telescopes, namely for iPTF 13ajg (P60 R -band data at MJD 56429 from Vreeswijk et al. 2014, excluded) and for PTF 09cnd (*Wise* R -band data at MJD 55089 from Quimby et al. 2011, excluded). The new measurements supersede the earlier ones.

3.11. On the Diversity of the Data Set

The data set used in this paper was collected from a diversity of facilities, and the photometry is derived with different pipelines and methods. The quoted uncertainties assess the quality of the photometry for each facility or measurement method. The contribution of the host galaxy light to the SN measured flux is taken into account and reflected in the quoted uncertainties. An exception to this is for the UV photometry (*Swift*), for which the contribution from the host galaxy is not subtracted, but should be minimal (Section 3.7). Often the filter transmission curves of similar filters are different for different facilities or catalogs for calibration, such as r , R , and R_c , for example. However, we did not correct for these differences because they depend on the source spectra and their evolution, and these differences are typically very small, normally well below 0.1 mag.

In Figures 18(a)–(e), all photometry are shown together. When enough data are available, the photometry from different telescopes can be directly cross-checked, and we do not find evident discrepancies. Further corrections to the photometry, such as foreground extinction and k -corrections, and their uncertainties, are described below.

3.12. Foreground Dust Extinction and k -corrections

We derive Galactic foreground optical extinction A_V using the maps of Schlafly & Finkbeiner (2011) through the Galactic Dust Reddening and Extinction Service at the NASA/IPAC Infrared Science Archive, assuming a standard extinction law

and an extinction to reddening ratio $A_V/E(B-V) = 3.1$.²⁹ The mean uncertainty in the Galactic foreground extinction A_V for our sample is 0.009 mag, and we do not include this uncertainty in the photometric budget. The adopted A_V values are listed in Table 1. We calculate the extinction A_λ at the central wavelength of each filter using the reddening curve of Cardelli et al. (1989) and including the update for the near-UV given by O'Donnell (1994). Both apparent and absolute magnitudes reported in this paper are corrected for Galactic foreground extinction.

Host-galaxy extinction is not considered. SLSN host galaxies tend to be faint and have low metallicity (Neill et al. 2011; Leloudas et al. 2015; Lunnan et al. 2015; Perley et al. 2016; Chen et al. 2017; Schulze et al. 2018), and therefore we expect them to have negligible dust extinction in the red bands, with possible regions that may be locally more dusty, affecting mostly the UV (e.g., Cikota et al. 2017). On the other hand, SN Ib/c host galaxies can show significant extinction (mean $\langle E(B-V) \rangle \sim 0.2$ and <0.6 mag for $\sim 80\%$ of Type Ic, Ib, and Ic-BL SNe; Taddia et al. 2015; Prentice et al. 2016), but determining it case by case for our comparison sample is often not possible and is beyond the scope of this paper.

We calculate the k -corrections K_{gr} for the SLSN sample from observed PTF r to rest-frame g (SDSS filter system) using spectral series of PTF 12dam and iPTF 13ajg (Vreeswijk et al. 2014, 2017; Quimby et al. 2018) and following Hogg et al. (2002). Using individual spectra for each SLSNe was not possible here, due to the paucity of sufficient spectral coverage at all epochs for the SLSNe in our sample. The spectral coverage of PTF 12dam is frequently sampled and spans from -25 to 321 rest-frame days after the peak, while the spectra of iPTF 13ajg are reliable until 60 days after peak. In the overlapping interval, there is good agreement between the k -corrections calculated from the two series of spectra. This indicates some level of similarity between the spectra, which is also confirmed by the spectral analysis of the PTF SLSN-I sample (Quimby et al. 2018). The spectra of the more slowly evolving SLSNe-I change more slowly. However, the k -corrections based on PTF 12dam and iPTF 13ajg are similar, so the differences in k -corrections for faster and slower SLSNe-I should be small. Given this similarity, and due to the general lack of spectral series as complete as those for PTF 12dam, we apply the k -corrections derived from the spectra of PTF 12dam and their evolution to all of the SLSNe in our sample.

The spectra were not warped to match the observed photometry of the individual SLSNe. This could have led to more accurate k -corrections. However, the uncertainty from the fact that we use the spectrum of PTF 12dam as a reference for the k -correction for all individual SLSNe is likely larger than the precision that could be gained by such a procedure. In addition, to make a reliable warping, photometry in at least two bands (and much preferably three) would be necessary, and this was not always available. The spectra of PTF 12dam were carefully flux calibrated. To ensure a smooth evolution of the k -correction with time, we interpolate the individual k -correction values and obtain a smooth k -correction evolution in time for each SLSN, through a third-order polynomial fit of the individual k -correction values.

The residuals from the third-order polynomial fit of the k -correction values with time can be used to estimate the

²⁹ The background and further cautionary notes are reported at <http://irsa.ipac.caltech.edu/applications/DUST/docs/background.html>.

uncertainties on the k -corrections, which are between 0.004 and 0.05 mag in our sample, with an average of 0.02 mag. These values show the scatter around the best-fit k -correction curve. Fitting the k -correction through individual points ensures that potential outliers, e.g., due to inaccurate flux calibration of the reference spectra, become negligible because the fit is driven by the majority of the points. The dominant source of uncertainty on the k -correction is likely the fact that we use the spectrum of PTF 12dam as a reference for the k -correction for all SLSNe, but this cannot be trivially estimated. Using different SLSN spectra as a reference for the k -correction in a different but comparable sample of SLSNe, the uncertainties on the k -corrections are 0.01–0.1 mag (Wiis 2017, private communication Table 4.1.1), although these are potentially slightly overestimated because they are derived with linear fits to the k -correction data. We do not include the uncertainties on the k -correction in our photometry uncertainty budget.

Table 9 lists the values of the adopted smooth k -correction at the epochs of the PTF 12dam spectra, applied to the redshifts of the SLSNe of our sample. Our k -correction values are in agreement with those of Nicholl et al. (2015b; $K_{gr} = -0.3$ before peak for LSQ 14bdq at $z = 0.347$). The k -corrections that we apply rely on the assumption that the spectra of our SLSN sample are similar to those of PTF 12dam out to late epochs. At late times, the assumption of similarity among the spectra is less certain. We therefore recommend exercising caution in trusting our k -corrections at late epochs.

For the comparison with the Ib/c sample at maximum light, we calculate the k -correction from the observed r to rest-frame r using the spectrum at the peak of PTF 10tqv and following Hogg et al. (2002). We then derive the rest-frame g by applying a color correction from the observed mean $g - r = 0.36$ mag of a large sample of Type Ib/c SNe of Prentice et al. (2016). Where necessary, we convert $B - V$ measurements from Prentice et al. (2016) at the V peak to $g - r$ and adopt the weighted average, and otherwise directly use the observed $g - r$ at the g peak. The standard deviation on the $g - r$ distribution is 0.34 mag (0.25 and 0.23 mag for the $g - r$ and $B - V$ distributions). Since $g - r$ evolves significantly for SNe Ib/c (e.g., Taddia et al. 2015; Prentice et al. 2016), the r to g conversion used here for SNe Ib/c is most reliable around SNe peaks.

4. Characterizing the Light Curves

The light curves of PTF H-poor SLSNe sometimes show complex features, such as bumps/plateau, double peaks, and a change of the decay rate. Besides, the data are often sparse. We use the following independent diagnostics to characterize different properties of the light curves.

1. *SN peak magnitudes*—derived with a second-order polynomial fit to the data around the peak (see Section 4.1).
2. *Early- and late-time decay rates*—derived with two independent linear fits to the data at early and late times after peak (see Section 4.2).
3. *Rise and fall times by 1 mag*, $t_{rise}^{\Delta 1 \text{ mag}}$ and $t_{fall}^{\Delta 1 \text{ mag}}$ —the times the SN takes to rise and fall by 1 mag from the peak (see Section 4.4), measured on light curves which have been smoothed using interpolation (see Section 4.3).
4. *Half-flux rise and fall times* $t_{rise,1/2}$, $t_{fall,1/2}$ —the times for the SN fluxes to rise from half-flux to peak, and to fall

form peak to half-flux (see Section 4.5), measured on light curves that have been smoothed using interpolation (see Section 4.3).

The derived quantities are listed in Table 8, and the details for each diagnostic are reported below.

4.1. Peak-magnitude Distribution

We calculate the absolute magnitudes using the distance modulus for a given z (e.g., Hogg 1999). At the z considered here (~ 0.3), the difference in distance modulus obtained from different cosmology models is negligible compared to the uncertainties in the observed apparent magnitudes. The redshifts of the SLSNe are derived in most cases to three decimal digits (see Table 1). In fact, here we are interested only in the relative luminosity distances between different SNe, and the relative uncertainties are even smaller. The uncertainties on the absolute magnitudes are therefore largely dominated by the uncertainties on the observed apparent magnitudes, and we do not make any attempt to include uncertainties due to the distance estimate.

We determine the peak times and magnitudes by fitting a second-order polynomial to the rest-frame g -band magnitudes around the maximum brightness, typically between –30 and 30 days around the approximate peak, or adjusting this interval to adapt to the data coverage. The fitted curves and the relevant time intervals are shown in Figures 18(a)–(e).

Figure 3, top panel, shows the peak-magnitude distribution of H-poor SLSNe (solid blue), Type Ic-BL SNe (shaded yellow), and Type Ib, Ic, and Ib/c SNe (solid orange), all from the PTF survey, for a brightness bin of 0.2 mag. Note that only SNe where the peak could be observed and constrained are included in this plot. When calculating the number of SNe for each brightness bin, it is important to consider the observational biases. Although SLSNe are bright enough to be observed at larger distances, many normal SNe could actually be exploding at those distances, but be too faint to be detected (Malmquist bias). To compare the numbers of SNe in a fair way, it is therefore necessary to normalize the numbers to the same comoving volume. We calculate the volumetric correction V_c for each SN as the ratio between the volume probed by the most luminous SLSN in our sample ($M_{g,\max} = -22.42$ mag at peak) and the volume probed by the individual SN, given the limiting magnitude of the PTF survey of $m_{\lim} = 20.5$ mag (Cao et al. 2016), i.e., the maximum luminosity distance at which each SN would have been observed with this limiting magnitude. The volumetric correction factor V_c is then expressed as follows:

$$V_c = V_{\max} / V_{\max,i} = \left(\frac{D_{L,\max}}{1 + z_{\max}} \right)^3 / \left(\frac{D_{L,\max,i}}{1 + z_i} \right)^3, \quad (1)$$

where the luminosity distance of the brightest SN in the sample is $D_{L,\max} = 10^{((m_{\lim} - M_{g,\max}) + 5)/5}$, and the luminosity distance for each individual SN is $D_{L,\max,i} = 10^{((m_{\lim} - M_{g,i}) + 5)/5}$. Figure 3, bottom panel, shows the peak-magnitude distribution after the volumetric correction. The mean peak magnitude of the SLSN sample is $\langle M_{g,\text{peak}} \rangle = -21.14$ mag with a standard deviation of 0.75 mag.

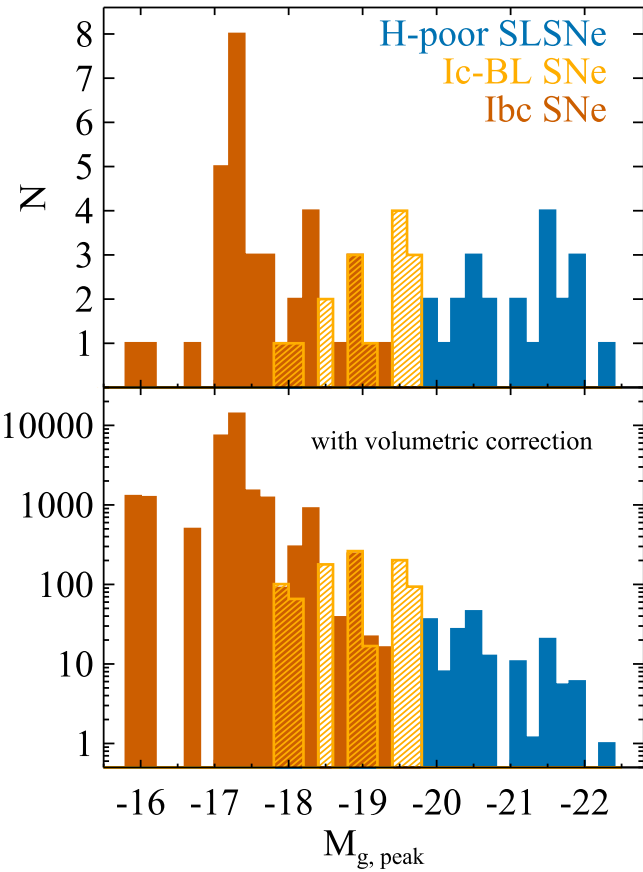


Figure 3. Peak-magnitude distribution of the labeled types of PTF SNe for rest-frame g absolute magnitudes. The bottom panel shows the peak-magnitude distribution after volumetric correction (i.e., corrected for Malmquist bias).

4.2. The Postpeak Early- and Late-time Decay Rates

The light curves of H-poor SLSNe can show a change in decay rate (e.g., Inserra et al. 2013). Here we independently characterize the postpeak early- and late-time decay rates of H-poor SLSNe with linear fits to the early-time and late-time data separately. We study the early decay with a linear fit to the rest-frame g magnitudes in a time interval between the peak and typically 60 days after peak. In some cases, this interval was adjusted to the data coverage, or to avoid changes of slope. The selected time intervals and the resulting linear fits to the data are displayed in Figures 18(a)–(e) (solid curves). We define the late-time decay as typically beyond 60 days after peak and characterize the decay rate with a linear fit to the data, in the same way as we did for the early-time decay. The linear fits to the late-time decays are displayed in Figures 18(a)–(e) (solid curves, typically beyond 60 days after peak).

Figure 4 shows the distribution of the early-time decay slopes (top panel) and the late-time decay slopes (bottom panel). SLSNe that were originally classified as sub-type R within the PTF survey are marked separately in this figure and compared to the rest of the sample. The original criterion for being classified as an SLSN-R was either a slow decline or spectral similarity with SN 2007bi, with no quantitative threshold. We do not intend to use these criteria as a meaningful classification, but rather to test this classification scheme, because it is often used in the literature (e.g., Gal-Yam 2012; Inserra et al. 2017).

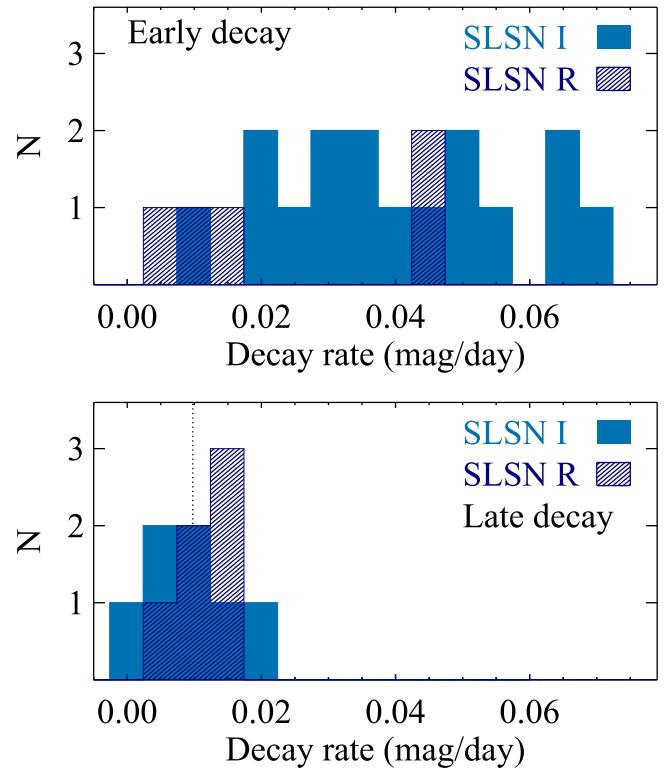


Figure 4. Postpeak decay slope distribution at early times (typically below 60 days, top panel) and at late times (typically beyond 60 days, bottom panel). At late times, all observed SLSNe cluster around the ^{56}Co to ^{56}Fe decay rate of $0.0098 \text{ mag day}^{-1}$ (dotted vertical line).

The decay rate of most SLSNe slows down from early to late times. The decay rates and the times of transition from a faster to a slower decay (the intersections between the early- and late-time linear fits) are reported in Table 8.

4.3. Light-curve Smoothing

We smooth the SN light curves to be able to further measure the rise and decay times more easily. We model the observed light curves with a nonparametric model, as follows. We first fit a first-order polynomial to the rest-frame g -band flux light curves locally. Then, we consider a fitting interval of 5 days (at phases until 5 days after peak), 10 days (at phases beyond 50 days after peak), and proportional to the phase (0.2 times) otherwise. For the interpolations, we use a Gaussian smoothing kernel that weights the fluxes according to their phase distance to each interpolated point. The smoothing algorithm also uses the uncertainties on the photometry to weight the data points. In order to avoid mathematical artifacts, a few auxiliary points are added to the observations. The light-curve smoothing algorithm is described in more detail in Rubin et al. (2016). In a few cases, to avoid unphysical wiggles in the smoothed light curves for poorly sampled regions, we binned scattered data during small time intervals. Namely, we binned the data for PTF 10aagc between 32 and 44 rest-frame days after peak; PTF 09cwl between 122 and 141; PTF 10vvg between 44 and 62; PTF 11rks at 55, and between 144 and 154; and PTF 12gty between 141 and 158. We adopt the formal error on the smoothed fluxes computed by the smoothing algorithm, and assume a minimum uncertainty of 10% of the flux in those cases where the formal errors are smaller.

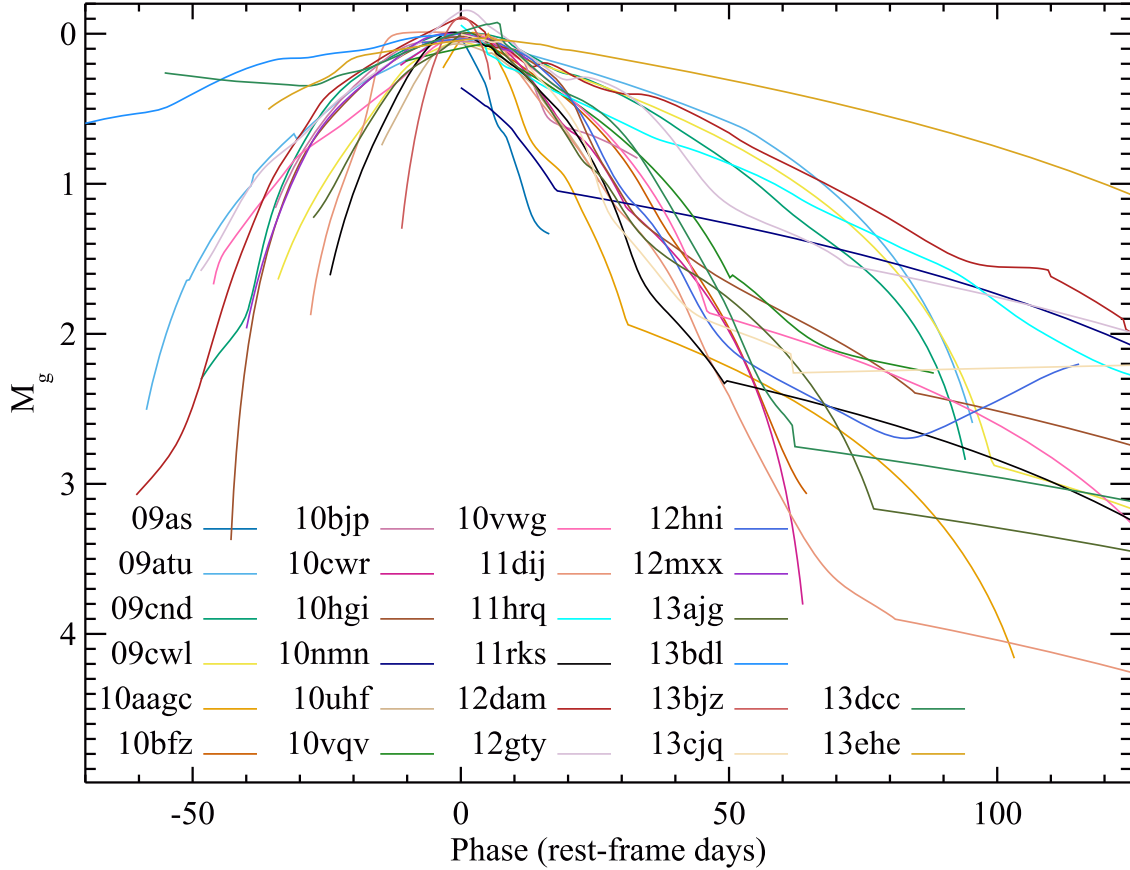


Figure 5. Rest-frame g -band smoothed light curves of the SLSNe in our sample, normalized at peak. PTF 10nmn is normalized with respect to the peak magnitude, which is taken from O. Yaron et al. (2018, in preparation) and is not presented in this paper. The peak magnitudes are derived with a second-order polynomial fit to the data (Figures 18(a)–(e)) and reported in Table 8.

The light-curve smoothing fits to the data in flux space, including the auxiliary points, are shown in Figure 19. The collection of all smoothed light curves, normalized by the peak magnitude, is shown in Figure 5. Even when normalized to the peak, there is a wide variety of light-curve behaviors among H-poor SLSNe, and the scatter is too large to reduce them to a single template. Remarkably, there is no clear gap between fast- and slow-decaying SLSNe.

4.4. Times to Rise and Decay by 1 mag from the Peak

We derive the times to rise (and decay) by 1 mag to (from) the peak, $t_{\text{rise}}^{\Delta 1 \text{ mag}}$ ($t_{\text{fall}}^{\Delta 1 \text{ mag}}$) by inspecting the smooth light curves (Section 4.3). Figure 20 displays the time intervals within 1 mag from the peak. Table 8 lists the resulting rise and decay times. The errors are estimated starting from the errors on the smoothed light curves (Section 4.3). We create a pseudo-random normal distribution of the smoothed flux errors around the smoothed light curves, through n Monte Carlo realizations, and we estimate n rise (and decay) times. We finally derive the uncertainties on the rise (decay) times from the standard deviation of the distribution of rise (and decay) times and assuming a minimum uncertainty of 2 days. We test for convergence of our results by varying the number of Monte Carlo realizations n between 10, 100, 1000, and 10,000, and eventually use $n = 1000$.

In Figure 6, we investigate the cross-correlations between $t_{\text{fall}}^{\Delta 1 \text{ mag}}$, $t_{\text{rise}}^{\Delta 1 \text{ mag}}$, their sum, and the peak magnitude. There is a clear correlation between $t_{\text{fall}}^{\Delta 1 \text{ mag}}$ and $t_{\text{rise}}^{\Delta 1 \text{ mag}}$.

We fit this correlation linearly, assuming $t_{\text{rise}}^{\Delta 1 \text{ mag}} = A + B \times t_{\text{fall}}^{\Delta 1 \text{ mag}}$ and including the observed uncertainties in both x and y axes, for each SN type. SNe where the data are not sufficient to constrain $t_{\text{rise}}^{\Delta 1 \text{ mag}}$ and $t_{\text{fall}}^{\Delta 1 \text{ mag}}$ are excluded from this fit, as reported in Table 8. The results of this fit are shown in Figure 6 (dotted curves) and reported in Table 2. We also compute the Pearson and Spearman correlation coefficients, which measure the strength (tightness and monotonicity) of a correlation not taking the observed uncertainty into account, and their null probabilities. These are listed in Table 2.

We also find a trend between the peak magnitudes and $t_{\text{rise}}^{\Delta 1 \text{ mag}}$, $t_{\text{fall}}^{\Delta 1 \text{ mag}}$, and the peak width.

4.5. Times to Rise and Decay by Half-flux

We further characterize the rise and decay times using the method of Prentice et al. (2016), who measured the time required to double or halve the flux with respect to the peak flux of a sample of stripped-envelope SNe (Ib/c). We derive $t_{\text{rise},1/2}$ and $t_{\text{fall},1/2}$, the time to double and halve the flux, respectively, for the PTF SN sample considered in this paper, using the smoothed flux light curves (Section 4.3). The resulting $t_{\text{rise},1/2}$ and $t_{\text{fall},1/2}$ are reported in Table 8. We calculated the uncertainties in the same way as for the rise and decay times by 1 mag (Section 4.4).

Figure 7 shows the comparison of $t_{\text{rise},1/2}$ and $t_{\text{fall},1/2}$ among the different samples and SN types, and compares it with the results of Prentice et al. (2016). We linearly fit the correlations between rise and decay times for each SN type in the same way

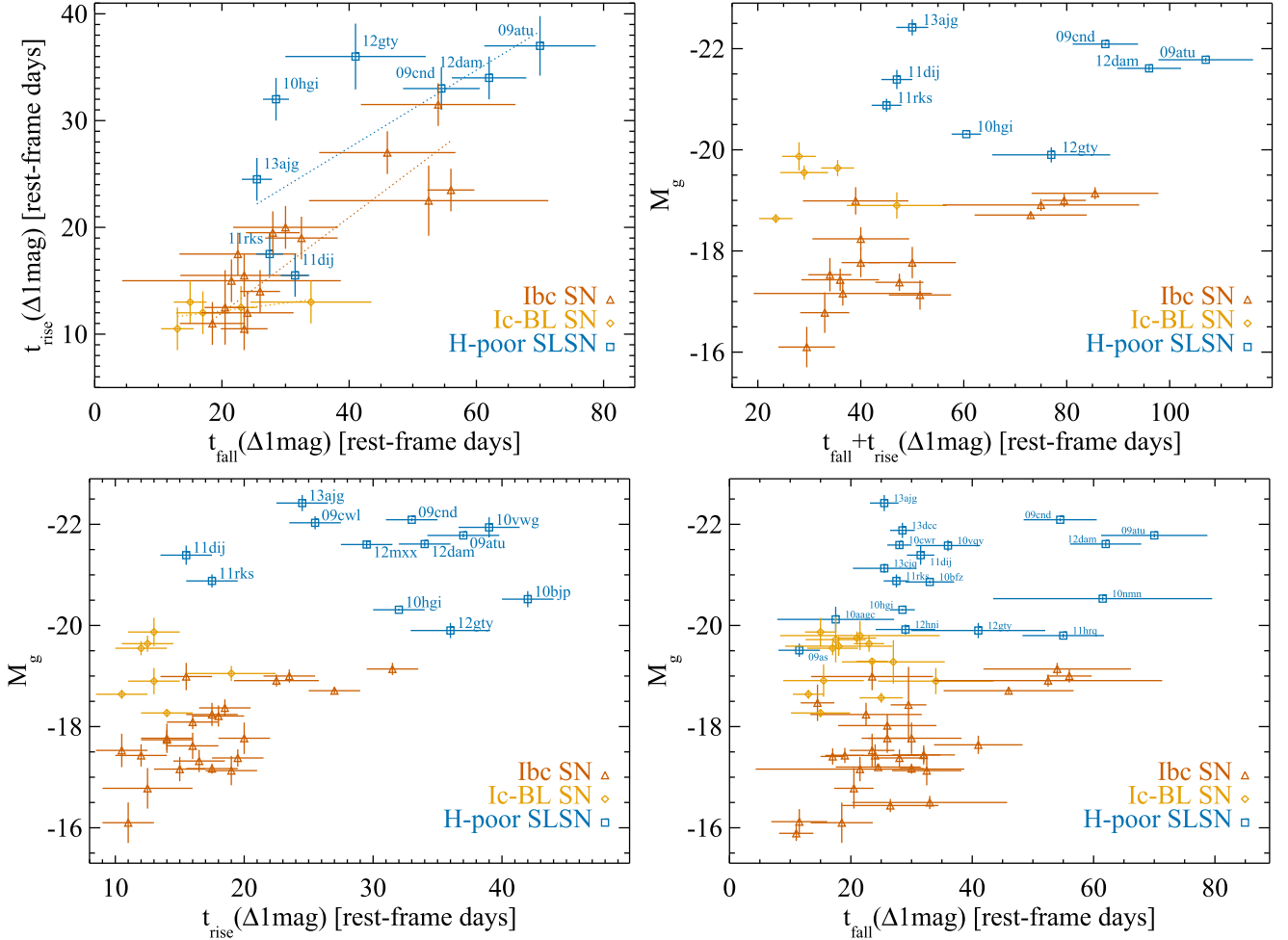


Figure 6. Times to rise and decay by 1 mag to and from the peak, and peak magnitudes (rest-frame g). The dotted curves show linear fits to the data in our sample. The bars show the typical uncertainties; see the text.

Table 2

Normalizations and Slopes of the Linear Fits of the Correlations between Rise Times and Decay Times (Figures 6 and 7)

Type	A	B	r	p_r	ρ	p_ρ
$t_{\text{rise}}^{\Delta 1 \text{ mag}} = A + B \times t_{\text{fall}}^{\Delta 1 \text{ mag}}$						
SLSN	12.93 ± 6.55	0.36 ± 0.15	0.69	0.057	0.76	0.028
$t_{\text{rise},1/2} = A + B \times t_{\text{fall},1/2}$						
SLSN	17.32 ± 6.22	0.21 ± 2.06	0.39	0.270	0.44	0.206

Note. r and ρ are the Pearson and Spearman correlation coefficients, respectively, and are listed with their respective null probability (p_r and p_ρ).

as for the rise and decay times by 1 mag (Section 4.4). The results of the fit are shown in Figure 7 (dotted curves) and reported in Table 2.

5. Discussion

In this paper, we study 26 hydrogen-poor SLSNe at “low” redshift ($\langle z \rangle = 0.27$), all spectroscopically classified as an SLSN-I and discovered by the (i)PTF survey. Here we characterize their light curves and discuss their (dis)similarity to SNe Ib/c and Ic-BL.

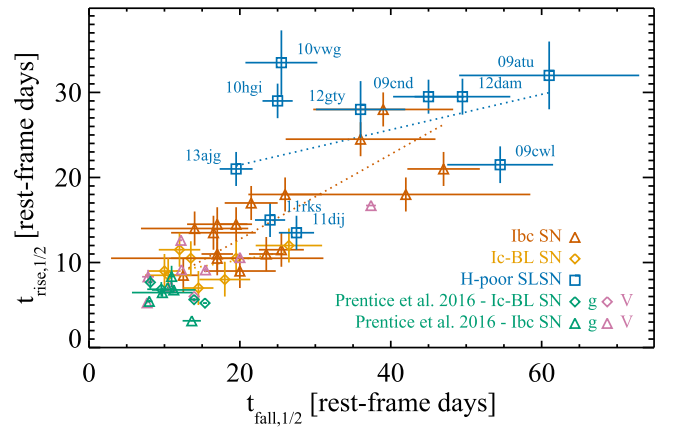


Figure 7. Times to rise and decay by half-flux. The dotted curves show the linear fit to the data in our sample.

5.1. Peak-magnitude Distribution

Figure 3, top panel, shows the distribution of the rest-frame g -band absolute peak magnitudes of SLSN, Ib/c, and Ic-BL. These SNe are all discovered by the PTF survey and separated into these three classes through spectroscopic classification (Quimby et al. 2018; Schulze et al. 2018). The k -correction has been applied as described in Section 3.12. Clearly, not all peak

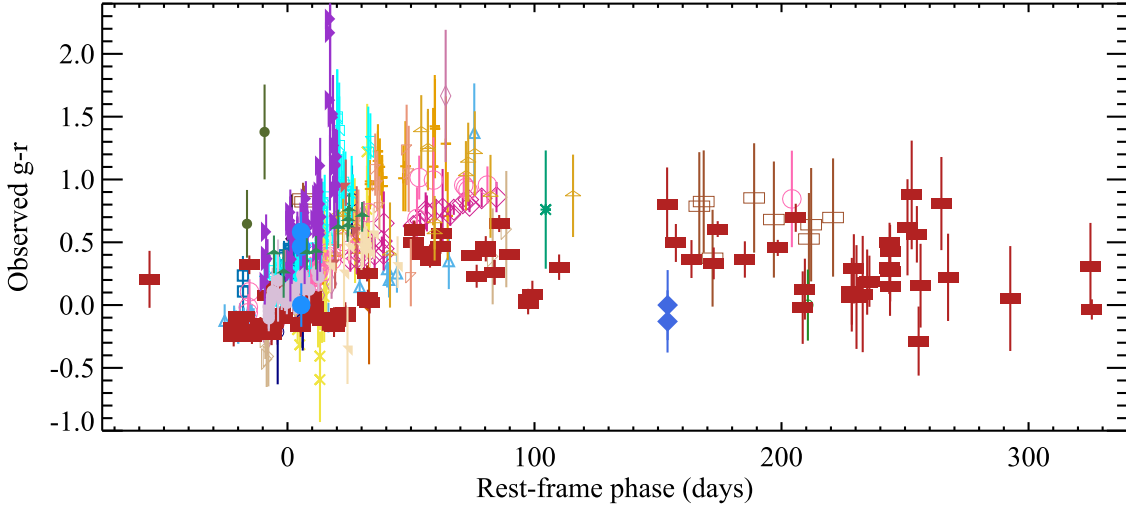


Figure 8. Observed $g - r$ color of the SLSNe in our sample. The symbols and colors are as in Figure 1.

magnitudes of SLSNe are brighter than < -21 mag. This threshold was an operational definition that was used to start characterizing SLSNe in the early days of their discovery (Quimby et al. 2011; Gal-Yam 2012). In fact, spectroscopically classified SLSNe-I from PTF span a wider range in absolute peak magnitudes, $-22.5 \lesssim M_{g,\text{peak}} \lesssim -20$ mag. The mean absolute peak magnitude in the PTF sample is $\langle M_{g,\text{peak}} \rangle = -21.14$ mag, with a standard deviation of 0.75 mag, which is about 2 and 4 mag brighter than the mean for SNe Ic-BL and Ib/c in our sample, respectively. The SLSN mean peak magnitude in the PTF sample is similar to what Lunnan et al. (2018) found for the higher- z sample from PS1, and thus we confirm no evidence for evolution of the SLSN peak luminosities with z on the currently available data.

Furthermore, the peak magnitudes of SLSNe-I are all brighter than SNe Ib/c. The gap between the brightest SN Ib/c and the faintest SLSN-I is of about 0.5 mag, although somewhat uncertain given the limited size of the samples and the uncertainty on the host-galaxy extinction for the SNe Ib/c. SNe Ic-BL are typically brighter than SNe Ib/c and fill this gap. The distribution of peak magnitudes is continuous from SNe Ib/c to SNe Ic-BL and SLSNe. There is very little overlap between the SLSN population and SNe Ic-BL.

It is crucial to take into consideration the fact that fainter SNe can be observed and counted only out to smaller distances. When applying the volumetric correction to compensate for this bias (Figure 3, bottom panel), the peak magnitude distribution decays smoothly and exponentially from SNe Ib/c to Ic-BL and to SLSNe. Another important bias to keep in mind is spectroscopic completeness. Because SNe Ib/c exist in the same parameter space as Type Ia or IIp SNe, some of them may be not selected for spectroscopic classification and therefore missing from those that we sample.

We conclude that the peak magnitudes of SLSNe are brighter than those of SNe Ib/c and Ic-BL. However, there is no evidence for SLSNe being drawn from a separate population when considering only the peak-magnitude distribution and taking the volumetric correction into consideration. Further evidence for the difference between SLSNe and SNe Ib/c comes from the rise and decay timescales, which we discuss in Section 5.4.

5.2. Observed Colors

Figure 8 shows the evolution of the observed $g - r$ color for individual SLSNe. The $g - r$ color seems to increase at early epochs, until a few tens of days after peak. The mean observed $\langle g - r \rangle$ at peak is 0.24 mag, with a standard deviation of 0.37 mag. At later times, the $g - r$ color evolution seems to stabilize at around ~ 0.5 mag, and perhaps higher.

This $g - r$ evolution in SLSNe is overall similar to that in SN Ib/c (see Figures 22–25 of Prentice et al. 2016). The $g - r$ color in SLSNe may, however, rise for a longer time (up to ~ 50 days after peak, while SNe Ib/c reach a plateau at 10–20 days after peak), and to lower $g - r$ (the color plateau in SNe Ib/c spans roughly between 0.5–1 mag). However, we caution against a direct comparison of the observed $g - r$ between nearby SNe and SLSN, given their higher redshift. Indeed, after k -correction, the rest-frame $g - r$ colors at peak in SLSNe span roughly between -0.6 and 0.0 mag. The observed-frame colors are reported here only as an observational reference. In Section 5.9, we further discuss rest-frame $g - r$ colors at peak in SLSNe.

5.3. Decay Rates

Figure 4 shows the postpeak decay rates at early times (top panel, typically before 60 days after peak) and late times (bottom panel, typically beyond 60 days after peak), as derived in Section 4.2. The two distributions are quite different, indicating that at early times, SLSNe decay faster than at late times. The mean SLSN decay rates are 0.04 and 0.013 mag day $^{-1}$ at early and late times, respectively, with standard deviations of 0.02 and 0.005 mag day $^{-1}$. All SLSNe with available data in our sample slow down their decay rate from early to late times. Moreover, their late-time decay rate settles around ~ 1 mag decay per 100 days. This rate is similar to the radioactive decay of ^{56}Co to stable ^{56}Fe (more specifically, 102.3 days mag $^{-1}$; Nadyozhin 1994; Wheeler & Benetti 2000). While at late times all SLSNe-I with available data show this slow decay, some selection biases may be present, because fast decays at late times may fall below the detection thresholds and not be measurable.

The late-time decays expected within the magnetar scenario can, under certain circumstances, mimic the radioactive ^{56}Co decay (e.g., Moriya et al. 2017). We further discuss this in Section 5.8.

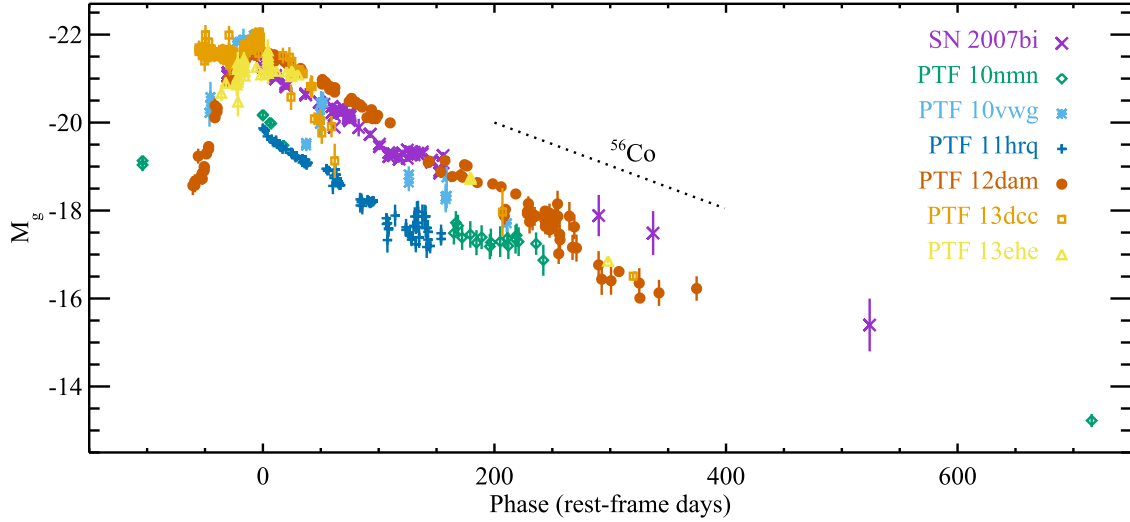


Figure 9. Rest-frame M_g light curves of the SLSNe originally classified as SLSNe of the R type.

The SLSN PTF 12hni is excluded from the late-time decay distribution because it exhibits a clear rebrightening (in all covered filters) and thus a negative decay rate, starting at about 75 days after peak, as reported in Table 8. This could represent a case where interaction with the CSM re-energizes the light curve at late times, through the transformation of kinetic energy into luminosity. This typically requires a high optical depth, and one may naively not expect to observe broad lines and absorption features in this case (see, however, Moriya & Tominaga 2012). The rebrightening of PTF 12hni was not covered by spectral observations (Quimby et al. 2018).

In Figure 4, we distinguish between classical H-poor SLSNe and those SNe originally classified as SLSNe-R within the PTF survey due to their slow decay early after the peak (consistent with radioactive decay, or spectrally similar to SN 2007bi). We stress again that we do not intend to use these criteria as a meaningful classification, but rather to test this classification scheme. At late times, the decay rates of SLSNe-R indeed cluster around the radioactive nickel decay rate, which is expected given the way SLSNe-R were originally selected. However, at early times, a couple of SLSNe-R have steeper decay slopes. Moreover, there is no evidence for a bimodal distribution in the decay properties in Figure 5, where all smoothed light curves are plotted together, after being normalized around the peak. Therefore, there is no clear separation between SLSNe-R and classical SLSNe-I. This casts doubt on the existence of SLSNe-R as a separate class, as initially suggested by Gal-Yam (2012).

Nevertheless, we note that early-time light-curve features are more common in SLSNe-R than in classical SLSNe-I. While none of the classical SLSNe-I show these features, three out of five SLSNe-R with early-time coverage (10nmn, O. Yaron et al. 2018, in preparation; 12dam and 13dcc, Vreeswijk et al. 2017) and possibly a fourth case (13ehe, Yan et al. 2015) have an early plateau or bumps of different strengths. At late times, the light-curve decay in SLSNe-R shows wiggles and bumps in virtually all events. Similar conclusions have also been drawn by Nicholl & Smartt (2016) and Inserra et al. (2017). In the case of the hybrid SLSN iPTF 15esb (late-time emergence of H emission), Liu et al. (2017) showed that the double peak of the light curves could be explained with a multiple-shell CSM interaction model. On the other hand, classical SLSNe-I might

show fewer late-time features, the only clear example being PTF 12hni and perhaps PTF 12gt, which are the least luminous among our sample. However, the paucity of late-time data for such events prevents us from drawing firm conclusions. For this reason, we keep open the possibility that two separate subclasses of SLSNe-I exist (slowly/rapidly declining), until further evidence is collected. The light curves of all potential SLSNe-R from PTF are shown together in Figure 9. The presence of bumps in the light curves indicate that either CSM interaction or multiple sources are responsible for powering the light curve, as also found by Vreeswijk et al. (2017) and Inserra et al. (2017).

5.4. Rise and Decay Times

In Figure 6, we compare the rise and decay timescales ($t_{\text{rise}}^{\Delta 1 \text{ mag}}$ and $t_{\text{fall}}^{\Delta 1 \text{ mag}}$; Section 4.4) and peak magnitudes for PTF SLSNe-I and PTF Type Ib/c and Ic-BL SNe.

The peak magnitudes are brighter for SLSNe-I than for SNe Ib/c and Ic-BL, as discussed in Section 5.1. We find possible mild trends between M_g and $t_{\text{rise}}^{\Delta 1 \text{ mag}}$ and between M_g and $t_{\text{fall}}^{\Delta 1 \text{ mag}}$, albeit with a very large scatter, and mostly when all SNe are considered. Indeed, neither luminous and fast-evolving events nor faint and slow-evolving ones are observed. A correlation between peak luminosity and rise time was observed for SNe IIn by Ofek et al. (2014a) and is consistent with the explanation of CSM interaction. The predictions for this correlation are in Ofek et al. (2014b).

The SLSNe in our sample tend to have longer rise timescales than SNe Ib/c; see below. Most SNe Ib/c and Ic-BL also tend to decay faster than SLSNe, although there are a few exceptions of slow-decaying, long-lived SNe Ib/c (e.g., PTF 11bo, also known as SN 2011bm; Valenti et al. 2012).

We find a correlation between $t_{\text{rise}}^{\Delta 1 \text{ mag}}$ and $t_{\text{fall}}^{\Delta 1 \text{ mag}}$ for SLSNe (Figure 6, top left panel). The parameters and strength of this correlation are reported in Table 2. Such a correlation is expected for both magnetar and nickel decay models (e.g., Nicholl et al. 2015a). This correlation is continuous and does not show two separate classes of SLSNe-I, in contrast to the findings of Nicholl et al. (2015a). Interestingly, SLSNe and “normal” SNe Ibc follow separate $t_{\text{rise}}^{\Delta 1 \text{ mag}}-t_{\text{fall}}^{\Delta 1 \text{ mag}}$ correlations. Although the correlation is not strong, there is an evident offset

toward longer rise times for SLSNe with respect to SNe Ib/c. The offset is roughly a 10 day longer rise timescale for SLSNe. Finally, this correlation has a large scatter, and moreover, in some cases (PTF 11dij and PTF 11rks), the measured rise and decay times are similar to those of SNe Ib/c. Therefore, the above-mentioned correlation cannot be used to distinguish between SLSNe-I and SNe Ib/c, but only as an indicator of the average properties of the two populations.

As a sanity check, we further study the rise and decay times with a different approach, by considering the time to rise and decay by half-flux from the peak ($t_{\text{rise},1/2}$ and $t_{\text{fall},1/2}$, Section 4.5). Again, the rise and decay times correlate continuously for SLSNe-I and the correlations are different for the three different classes of SNe. (The parameters and strength of this correlation are reported in Table 2.)

The difference between the correlations of the rise with the decay timescales for SLSNe and SNe Ib/c (and Ic-BL) is evident using both independent methods ($\Delta 1$ mag and half-flux). This suggests that SLSNe have longer rise timescales than SNe Ib/c, even for similar decay timescales. Observationally, we conclude that SLSNe show overall different light-curve properties from SNe Ib/c and Ic-BL. Therefore, SLSNe can be considered as a separate population, not only from a spectroscopic (Quimby et al. 2018) but also from a photometric perspective.

5.5. Bolometric Correction

We use the spectral information derived from a well-observed event to estimate the bolometric luminosity L_{bol} from single-band photometry. We adopt the conversion from the rest-frame g band to the bolometric luminosity derived for PTF 12dam by Vreeswijk et al. (2017) up to 334 rest-frame days after peak. The bolometric light curve of PTF 12dam was constructed from the observed spectral series and blackbody models of the UV/optical data. More details on this derivation are explained in Vreeswijk et al. (2017). We apply the bolometric correction from absolute magnitudes to the bolometric luminosity of PTF 12dam to all SLSNe in our sample, i.e., by basically adding a constant to the rest-frame g -band absolute magnitudes, where this constant evolves with the SN phase. This is valid under the assumption of spectral similarity among SLSNe-I. While there are strong indications for such similarity in our sample (Quimby et al. 2018), this is not always guaranteed, especially at late times when the spectral coverage is typically poorer than around peak. A solid case-by-case bolometric correction can in principle only be attempted for the few best observed cases with sufficient spectral coverage. Due to the paucity of such complete data sets, this cannot be done for the full sample and is beyond the scope of the current paper. Nevertheless, given the overall similarity among the spectra in our sample, it is still informative, as a first approximation for the study of the energetics, to use a simple bolometric correction to derive the bolometric luminosities. Because the relative shapes of the light curves does not change between different SLSNe in bolometric luminosity, we do not show the individual light curves. We report the bolometric luminosities at peak in Table 3. The total radiated energy is then derived by integrating the bolometric light curves. Because the bolometric light curves are defined over a limited time interval, the derived radiated energies are lower limits.

Table 3
Radiated Energy and Nickel Mass Estimates from the Peak Luminosity and the Late-time Decay

PTF ID	$\log L_{\text{bol,peak}}$ (erg s $^{-1}$)	$\log E_{\text{rad}}$ (erg)	$M_{\text{Ni,peak}}$ (M_{\odot})	$M_{\text{Ni,decay}}$ (M_{\odot})
09as	43.4	≥ 49.3	≤ 3.4	...
09atu	44.3	≥ 51.2	≤ 28.3	...
09cnd	44.5	≥ 51.3	≤ 37.3	≤ 5.5
09cwl	44.4	≥ 51.2	≤ 33.7	≤ 5.5
10aac	43.7	≥ 50.0	≤ 6.5	...
10bfz	44.0	≥ 50.4	≤ 12.1	...
10bjp	43.8	≥ 50.5	≤ 8.8	...
10cwr	44.3	≥ 50.8	≤ 23.5	≤ 1.0
10hgi	43.7	≥ 50.5	≤ 7.2	≤ 1.7
10nmn	43.7	≥ 50.6	≤ 8.3	≤ 4.5
10uhf	43.9	≥ 50.3	≤ 9.8	...
10vqv	44.2	≥ 50.8	≤ 21.4	≤ 6.0
10vwg	44.4	≥ 51.2	≤ 32.0	≤ 5.0
11dij	44.2	≥ 50.8	≤ 21.0	≤ 0.9
11hrq	43.6	≥ 50.2	≤ 6.2	≤ 3.1
11rks	43.9	≥ 50.6	≤ 10.7	≤ 2.7
12dam	44.3	≥ 51.2	≤ 24.6	≤ 9.7
12gtv	43.7	≥ 50.5	≤ 5.9	≤ 2.4
12hni	43.6	≥ 50.1	≤ 4.8	≤ 0.8
12mxx	44.2	≥ 50.8	≤ 22.6	...
13ajg	44.6	≥ 51.2	≤ 49.5	≤ 5.4
13bdl	43.9	≥ 50.6	≤ 9.6	...
13bjz	44.0	≥ 50.0	≤ 12.1	...
13cjq	44.1	≥ 50.7	≤ 15.2	≤ 3.4
13dcc	44.5	≥ 51.3	≤ 48.6	≤ 5.0
13ehe	44.2	≥ 51.2	≤ 18.3	≤ 6.5

5.6. Ni Masses

We investigate whether the peaks and light curve decays of SLSNe-I could be powered by Ni decay, using two independent methods. First, we derive a very rough estimate of what the required nickel masses would be if the SN peaks were completely powered by nickel. We use the relation $L_{\text{peak}} = \alpha E_{\text{Ni}} = (6.45 \times 10^{43} e^{-(t_{\text{peak}}/\tau_{\text{Ni}})} + 1.43 \times 10^{43} e^{-(t_{\text{peak}}/\tau_{\text{Co}})}) \times M_{\text{Ni}} / M_{\odot}$ (Nadyozhin 1994; Stritzinger & Leibundgut 2005), where $\tau_{\text{Ni}} = 8.8$ days and $\tau_{\text{Co}} = 111.3$ days, and assume no deviation from the Arnett rule ($\alpha = 1$, Arnett 1979). The time of explosion is quite uncertain in our sample, because the rise times are often not well-covered.³⁰ Thus, we use a representative $t_{\text{peak}} = 70$ days. For a few SLSNe-I that show indications for a longer rise time, we assume an explosion time of 100 days before peak (namely for PTF 10nmn, PTF 11hrq, and PTF 13dcc), and we assume the literature explosion time of 66 days before the peak for PTF 12dam (Vreeswijk et al. 2017). The uncertainties in this Ni mass calculation are of about 20% for an uncertainty in explosion date of about 30%. The Ni mass that we derive with this method for PTF 12dam is similar to what has been derived by Vreeswijk et al. (2017) with a more detailed Ni decay model of the full light curve. In this exercise, the main assumption is that the light curves are totally powered by radioactive Ni decay, while in fact there may be a significant contribution from CSM interaction, magnetars, or other sources. The derived nickel masses are therefore upper limits of the true values, for a peak time of 70 days after explosion. The results are reported in Table 3.

³⁰ In most cases, the SN empirical-model fit of Bazin et al. (2011) does not provide satisfactory results.

Second, we derive what the required nickel masses would roughly be if the SN late-time decay would be completely powered by nickel. In this case, we compare the SLSN decay, if sufficient photometry is available, to the decay of SN 1987A. For this SN, the well-studied decay is thought to be powered by the radioactive decay of $0.07 M_{\odot}$ of ^{56}Ni (Fransson & Kozma 2002; Seitzenzahl et al. 2014). To compare the SLSNe light curves with SN 1987A, we assume an explosion date for the SLSNe and shift the bolometric light curves to that of SN 1987A (taken from Pun et al. 1995), using the same method as Gal-Yam et al. (2009). We shifted the light curve of SN 1987A to match the potential transition from the diffusive phase to the radioactive decay in the SLSN light curves or to the late-time decay. The explosion dates are quite uncertain. We assume the same explosion dates as discussed above. While the assumption on the explosion dates are not secure, here we are only interested in a zero-order estimate of the Ni masses from the tails. Figure 10 shows the comparison between the SLSN light curves and SN 1987A. The Ni masses derived from the light-curve decay are labeled on the figure and reported in Table 3. These masses are upper limits, because they are calculated assuming that the late-time light curves are powered only by radioactive Ni, with no other contribution. The typical uncertainties on these nickel masses are large, roughly of the order of 50% (accounting for a shift in explosion date of up to 100 days). Despite the large uncertainties, these estimates are useful for the comparison with the nickel masses derived from the peaks.

In Table 3, we compare the nickel masses that we derived above with the two methods, one based purely on the peak luminosity and one based purely on the late-time decay. It is evident that the nickel masses derived from the peak luminosities are much higher than the nickel masses derived from the SN decay, both for fast- and slow-evolving SLSNe-I. This suggests that the SLSN peaks are not powered by nickel. This confirms the results of Inserra et al. (2013). In addition, the large ejecta masses required for powering the SLSN-I peaks with Ni radioactivity would increase the diffusion times, and therefore the light curves would show broader peaks than what is observed. A different component, such as magnetar spin-down or CSM interaction, is likely causing the high peak luminosities of most SLSNe-I. A factor of 5 discrepancy between the Ni masses required for the peak and the late-time decay was also found for SN 1998bw, which was possible to reconcile only with asymmetry of the ejecta (Dessart et al. 2017). Strong evidence for asphericity of this event, based on the spectra, was found by Mazzali et al. (2001) and Maeda et al. (2002, 2006). If asymmetry is relevant for SLSNe-I as well, the discrepancy between the nickel masses derived from the peak and the late-time decay may be partly mitigated (perhaps by a factor of 5 for asymmetries levels similar to SN 1998bw).

When data coverage is available, we observe a late-time decay of SLSNe-I, which is close to the radioactive decay of ^{56}Co to stable ^{56}Fe , as observed from the late-time decay slopes (Section 4.2). The nickel masses derived from this late-time decay are between ≤ 1 and $\leq 10 M_{\odot}$. This suggests that while nickel production is not the main source powering the light curve peaks, a nickel component could be important, and perhaps dominant, at late times. While the derived Ni masses are upper limits, producing up to $10 M_{\odot}$ of Ni is challenging in classical SN models. The PISN model can produce $1\text{--}10 M_{\odot}$

nickel from progenitor stars with cores of $90\text{--}105 M_{\odot}$ (Heger & Woosley 2002).

In the case of PTF 10hgi, the only data point at late times seems fainter than what would be predicted from the decay rate of ^{56}Co (Figure 10). The current ^{56}Ni mass estimated from the light-curve decay is $M_{\text{Ni}} \sim 2 M_{\odot}$. However, estimating the Ni mass directly by scaling the SN 1987A light curve to the fainter data point at late times would provide $M_{\text{Ni}} \sim 0.2 M_{\odot}$.

5.7. Radioactive Decay

One potential power source of SLSN-I light curves is radioactive decay of ^{56}Co to stable ^{56}Fe (e.g., Gal-Yam et al. 2009). The half-life time of the ^{56}Co decay is 77.2 days (Junde et al. 2011). As we discussed above, it is rather unlikely that the SLSN peaks are powered by radioactive decay because of the discrepancy between the Ni masses required by the peak luminosities and those required by the late-time decays. One possibility is that the late-time light curves are powered by radioactive decay. Indeed, we showed in Section 4.2 that whenever observable, the SLSN-I light curves tend to slow down, and at late times settle around the $0.01 \text{ mag day}^{-1}$ decay rate, which is typical of radioactive ^{56}Co decay with full trapping. On the other hand, Inserra et al. (2017) argued that SLSNe tend to decay faster than the radioactive rate, and therefore could not easily be associated with ^{56}Co decay. However, the escape of γ -rays can increase the decay rate. In this section, we investigate under which conditions γ -ray escape can efficiently induce a light-curve decline that is faster than the nominal radioactive decay rate.

The radioactive decay energy (RDE) deposition is the heating/excitation/ionization of the SN ejecta because of radioactive emission of γ -rays (and e^+) and the subsequent acceleration of electrons through Compton scattering (Jeffery 1999). This phenomenon is important for SNe Ia as well as for core-collapse SNe. After a diffusion phase when the γ -rays are fully trapped, a transition to a quasi-steady state marks the beginning of a regime where the decay is dominated by RDE deposition (and the diffusion timescale is much larger than the dynamical and radioactive timescales). At the transition point, the SN luminosity is purely determined by the total amount of radioactive material. The quasi-steady state decay is then exponential, starting with a radioactive slope that corresponds to full trapping. In time, the γ -rays can start to escape, and the decay can appear faster. We investigate here whether γ -ray escape is important for massive star progenitors.

We simulate the quasi-steady state decay from pure RDE deposition for stars with a density profile that has an inner plateau and decays exponentially (similar to the “s25e12” profile of Dessart & Hillier 2011), where the ^{56}Ni mass is distributed in the inner ejecta. We consider total ejecta masses between 25 and $100 M_{\odot}$, ^{56}Ni masses between 5 and $20 M_{\odot}$, and maximum expansion velocity between $10,000$ and $20,000 \text{ km s}^{-1}$. The total ejecta mass and maximum expansion velocity determine the absolute value of the density profile at each point. These simulations cannot treat the diffusive phase, but only the light-curve decay beyond maximum light and beyond the transition to the quasi-steady state. As a sanity check, we reproduce the observed radioactive light-curve phase of SN 1987A given an expansion velocity of 6000 km s^{-1} , the same density profile as we used for SLSNe, total ejecta mass of $10 M_{\odot}$, and $M(^{56}\text{Ni}) = 0.07 M_{\odot}$.

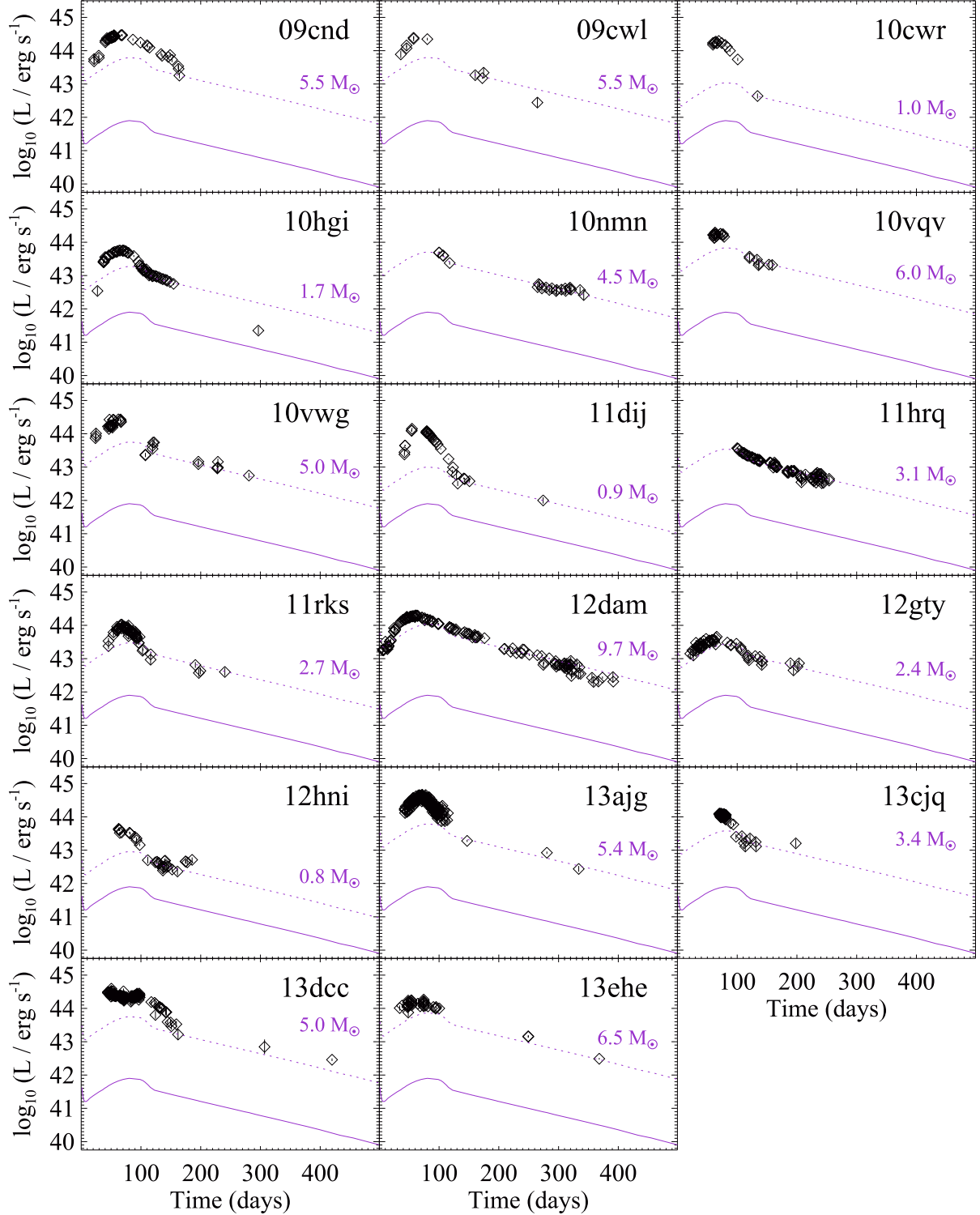


Figure 10. Bolometric light curve of SN 1987A (solid curve) is scaled (dashed curves) to match the decay of SLSNe-I (black diamonds) at late times, after bolometric correction. The M_{Ni} roughly estimated from this comparison are labeled. The time reference is in rest-frame days after explosion.

Figure 11 shows the resulting light curves of our RDE deposition simulations for different initial parameters. In all cases, we observe $\sim 100\%$ gamma-ray trapping at ~ 150 days after the explosion. At later times the luminosity can decrease more rapidly because of the reduced trapping due to lower densities. This effect is stronger for high expansion velocities and high $M_{\text{Ni}}/M_{\text{ej}}$ ejected masses. Within this set of simulations, the deviation from a pure radioactive ^{56}Co decay

ranges from 0.01 (still fully trapped) to a maximum of 0.27 mag ($\sim 50\%$ escape fraction) at about 450 days after explosion, with a decay rate of 1.33 mag in 100 days.

The contours in Figure 12 show the energy deposition fraction (where 100% means full trapping) from our RDE deposition simulations for the cases of 5 and 10 M_{\odot} of nickel. These results confirm that massive star progenitors, with high SN ejecta velocities and high Ni fraction in the ejecta, have

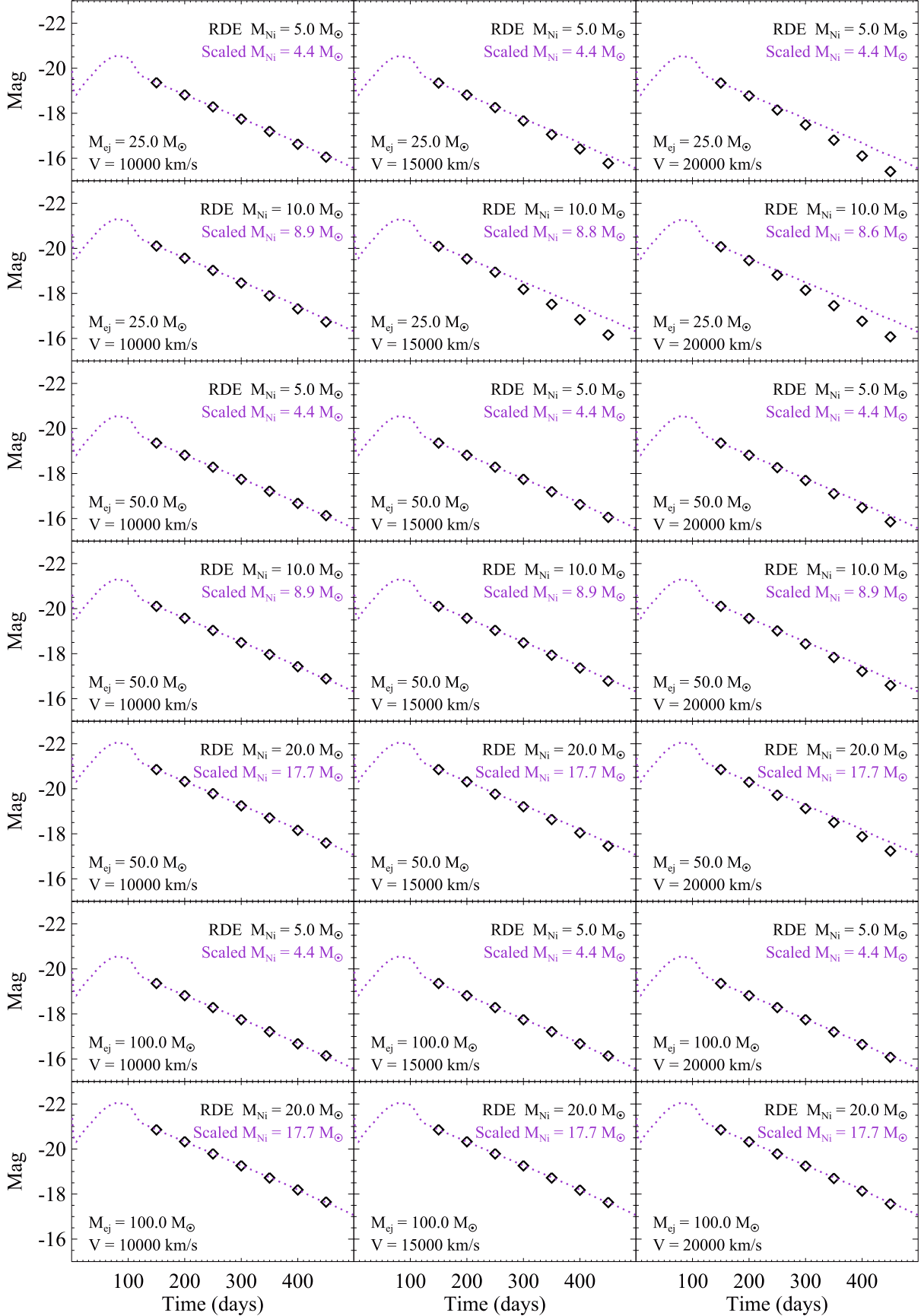


Figure 11. Simulated light curves using RDE deposition (black diamonds) for stars with different initial parameters (black labels). A comparison with the SN 1987A light curve, scaled up to match the simulated magnitudes at 150 days, and the associated Ni masses are shown (purple label and dotted curve). Time is measured in rest-frame days after explosion.

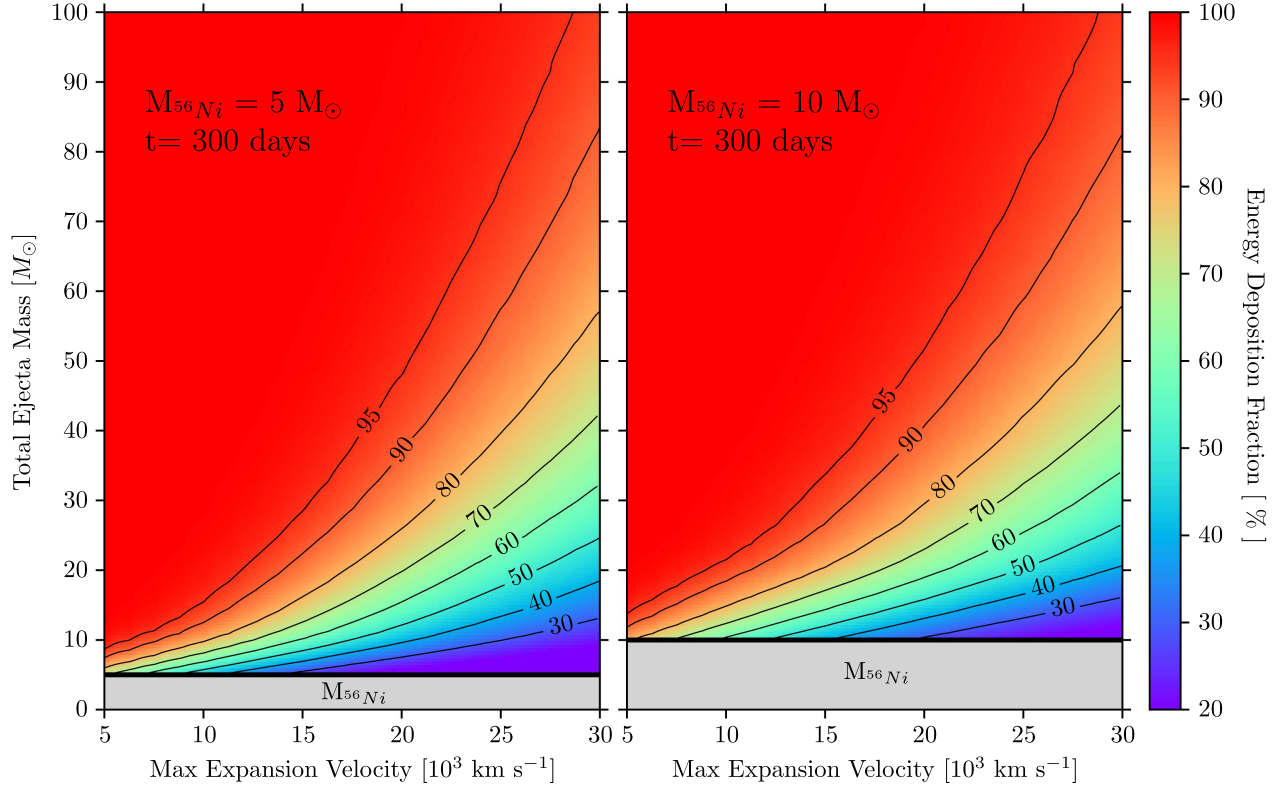


Figure 12. Contours show the energy deposition fraction (100% means full trapping) for different ejecta velocities and total ejecta masses, and in the cases of 5 and $10 M_{\odot}$ of nickel (left and right panels, respectively). The color scale displays an interpolation of the contours.

limited trapping and therefore can decay faster than the radioactive exponential decline. Figure 12 can also be used to roughly estimate the total ejecta masses in case the expansion velocity and trapping are known from the spectra and light curves, respectively.

An additional factor that can efficiently limit the trapping (and induce faster decays) is the potential mixing of ^{56}Ni in the outer layers. While this can be a dominant effect, we do not attempt to model it here, because this is highly dependent on the geometry of the mixing, which cannot be constrained.

5.8. Magnetar Modeling

We investigate whether the SLSN-I light curves could be powered by the spin-down of a magnetar. We consider an analytic magnetar model sourced from Arnett (1982) and Kasen & Bildsten (2010). The fitting technique is described in detail in A. Rubin et al. (2018, in preparation). The main model parameters are the initial pulsar spin P , the magnetic field B , the diffusion timescale $t_m \approx M_{\text{ej}}^{3/4} E_k^{1/4}$ (where M_{ej} and E_k are the ejected mass and kinetic energy, respectively), and the explosion time t_{exp} . This is a basic modeling that includes neither photon escape nor multiple components. The uncertainties are derived with a Monte Carlo treatment and shown in Figure 22. The treatment of the opacity is the same as in Inserra et al. (2013).

Figure 21 shows a fit of the magnetar model described above to the bolometric SLSN-I light curves. The best-fit parameters are reported in Table 4 and displayed in Figure 13. In most cases, we obtain a satisfactory overall description of the light curves, with the exception of PTF 10hgi, PTF 10vvg, and PTF 11rks, for which we observe a different decay than predicted from our magnetar fit. In addition, the magnetar

Table 4
Resulting Parameter from a Magnetar Fit to the Bolometric Light Curves

ID	B (10^{14} G)	P (ms)	τ_m (days)	t_{exp} (days)	$12 + \log$ [O/H] (PP04 N2)
09cnd	$1.56_{-0.11}^{+0.12}$	$1.30_{-0.18}^{+0.16}$	$63.0_{-3.0}^{+3.2}$	$-45.0_{-1.0}^{+1.0}$	$8.22_{-0.15}^{+0.09}$
09cwl	$2.24_{-0.20}^{+0.27}$	$1.31_{-0.39}^{+0.42}$	$57.7_{-8.1}^{+6.2}$	$-37.1_{-2.2}^{+4.4}$...
10bjp	$2.40_{-0.55}^{+0.87}$	$4.63_{-0.84}^{+0.29}$	$38.3_{-7.0}^{+8.8}$	$-46.6_{-2.6}^{+3.0}$	$8.14_{-0.10}^{+0.06}$
10cwr	$9.41_{-0.90}^{+0.67}$	$0.06_{-0.03}^{+0.10}$	$34.8_{-1.0}^{+0.9}$	$-12.6_{-0.8}^{+0.6}$	$7.96_{-0.24}^{+0.12}$
10hgi	$3.64_{-0.13}^{+0.13}$	$4.82_{-0.21}^{+0.21}$	$39.0_{-2.1}^{+1.9}$	$-42.0_{-1.3}^{+1.1}$	$8.27_{-0.06}^{+0.05}$
10nnm	$1.78_{-0.04}^{+0.04}$	$0.89_{-0.22}^{+0.40}$	$48.5_{-1.9}^{+2.4}$	$-104.7_{-1.0}^{+0.4}$	$8.16_{-0.04}^{+0.03}$
10vqv	$2.10_{-0.14}^{+0.17}$	$3.22_{-0.30}^{+0.30}$	$29.9_{-4.9}^{+6.1}$	$-28.5_{-2.3}^{+2.3}$	$8.28_{-0.05}^{+0.04}$
10vvg	$2.60_{-0.43}^{+0.55}$	$2.72_{-0.48}^{+0.43}$	$29.1_{-4.8}^{+6.5}$	$-34.1_{-7.1}^{+2.8}$...
11dij	$5.18_{-0.46}^{+0.65}$	$0.93_{-0.41}^{+0.39}$	$39.2_{-1.3}^{+1.4}$	$-27.6_{-0.8}^{+0.4}$	$7.93_{-0.20}^{+0.10}$
11rks	$4.15_{-0.43}^{+0.51}$	$4.40_{-0.43}^{+0.28}$	$26.7_{-1.7}^{+1.7}$	$-22.8_{-1.3}^{+1.1}$	$8.14_{-0.18}^{+0.13}$
12dam	$1.38_{-0.05}^{+0.05}$	$1.68_{-0.32}^{+0.08}$	$76.8_{-2.2}^{+2.1}$	$-56.0_{-0.8}^{+0.8}$	$8.07_{-0.01}^{+0.01}$
12gty	$2.62_{-0.25}^{+0.27}$	$5.36_{-0.32}^{+0.25}$	$54.0_{-4.2}^{+4.1}$	$-58.5_{-2.3}^{+2.0}$...
12mxx	$1.13_{-0.19}^{+0.26}$	$2.59_{-0.16}^{+0.08}$	$44.3_{-4.2}^{+5.0}$	$-48.4_{-1.9}^{+2.1}$	$8.19_{-0.19}^{+0.13}$
13ajg	$1.98_{-0.08}^{+0.08}$	$1.73_{-0.09}^{+0.09}$	$33.8_{-1.3}^{+1.3}$	$-28.7_{-0.8}^{+1.4}$...

Note. The last column lists the host-galaxy metallicity from Perley et al. (2016).

model does not describe well the light curve of PTF 11dij, both for the late-time decay and the early rise.³¹ The confidence levels of the best-fit parameters are shown in Figure 22.

Recently, Nicholl et al. (2017) have modeled a large literature SLSN-I sample with a magnetar model, including

³¹ Forcing the explosion date to be before -28 days improves the fit at late times, but cannot well explain the data around peak and at ~ 50 days after peak.

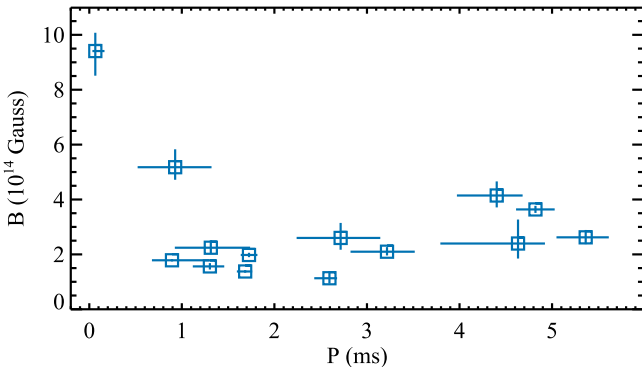


Figure 13. Magnetic field strength and magnetar initial spin, as listed in Table 4.

several published (i)PTF objects. The spin values P that we obtain are mostly consistent with the values of Nicholl et al. (2017). For PTF 12dam, we find a spin value $P = 1.87^{+0.07}_{-0.08}$ ms, which is a bit lower than the ~ 2.3 ms values that were derived by Nicholl et al. (2017) and Vreeswijk et al. (2017), and also lower than that by Chen et al. (2015). The magnetic fields B that we obtain are in all cases higher than what was derived by Nicholl et al. (2017). For PTF 13ajg, our B value is more similar to that found by Vreeswijk et al. (2014). For PTF 12dam, our B value is more similar to those found by Chen et al. (2015) and Vreeswijk et al. (2017).

The late-time luminosities expected from the spin-down of a magnetar decline as t^{-2} (e.g., Woosley 2010). In principle, such model may also be able to mimic the ^{56}Co decay of about 1 mag per 100 days, which we observe in SLSN-I late-time light curves. In the case of pure dipole radiation, the magnetar light curves start to have the same decay rate around 200 days postpeak. At later times, e.g., 400 days postpeak, the magnetar model is expected to have a decay rate that is noticeably slower than 1 mag/100 days (e.g., Inserra et al. 2013). However, the capability of a magnetar to mimic radioactive decay would require a pure dipole radiation and a narrow set of fine-tuned parameters, in particular for the magnetic field and Ni masses (Moriya et al. 2017). In Figure 14, we display the space parameter where a magnetar (in the dipole case) can mimic the radioactive ^{56}Co decay from Moriya et al. (2017), and compare it with the results from our magnetar fit on the SLSN light curves. The reference time intervals are derived from the observed times after peak where the SLSN decay follows the radioactive rate (Figure 10) and using the explosion times from the magnetar fits to the data (Figure 21). The magnetic field B is taken from the magnetar fit, while the Ni masses are taken from scaling the late-time light-curve decays (Section 5.6). The SLSNe for which these measurements are available are lying in the parameter space where the magnetar decay mimics the radioactive decay of ^{56}Co , with the marginal exception of PTF 11rks, for which a magnetar model does not describe the data well. Given that we do observe radiative-like light-curve decays at late times in SLSNe, it is perhaps not surprising that most of the derived magnetar parameters that we derive fulfill the radiative-mimicking criteria. These results indicate that we cannot disentangle between the magnetar and the radioactive decay models at these epochs, up to 400 days after explosion, but that observations at later times can be extremely powerful in disentangling between the two models.

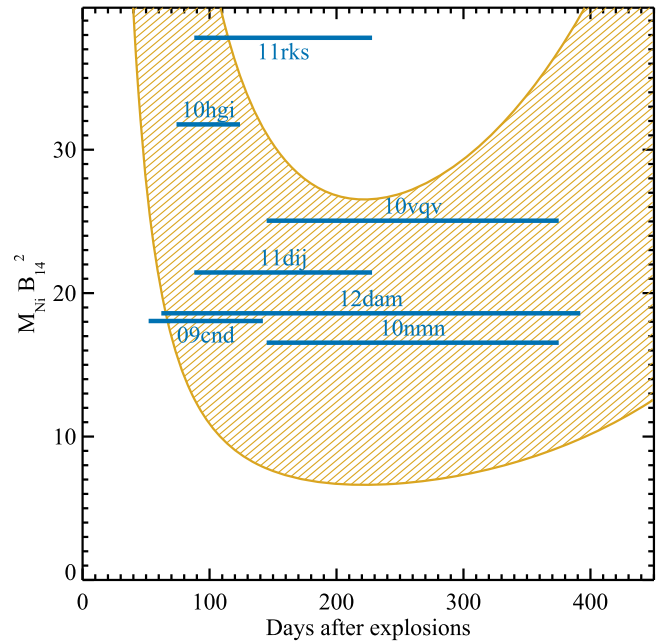


Figure 14. Parameter space where a magnetar (in the dipole case) can mimic the radioactive ^{56}Co decay (shaded area; Moriya et al. 2017). The horizontal lines mark the epochs when SLSNe are observed to decay consistently with radioactive decay.

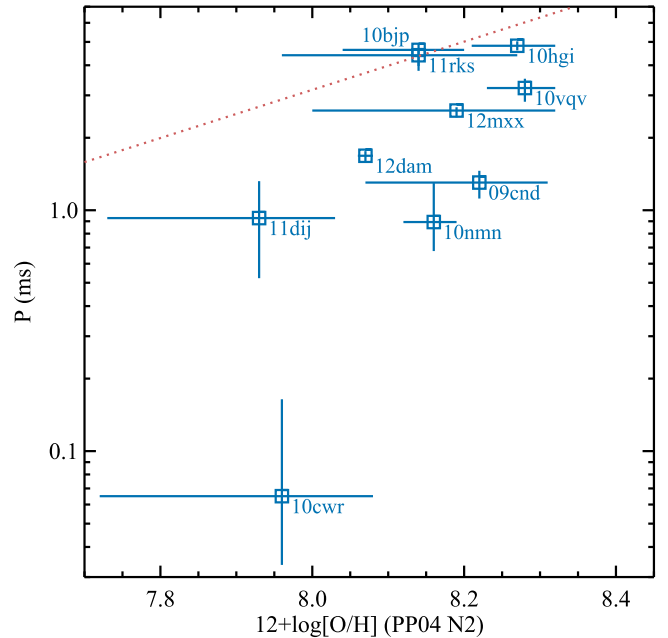


Figure 15. Magnetar spin and host-galaxy metallicity. The red dotted line shows the spin-metallicity correlation found by Chen et al. (2017).

Intriguingly, a correlation between the magnetar initial spin and the host galaxy metallicity was found by Chen et al. (2017). In Figure 15, we show these quantities for our SLSN data using the host metallicities derived in Perley et al. (2016; PP04 N2 scale) and compare them to the correlation of Chen et al. (2017). We cannot confirm the existence of such a correlation in the PTF sample, or at least we find a large scatter (more than a factor of 10) in the derived spin periods, for a similar metallicity range.

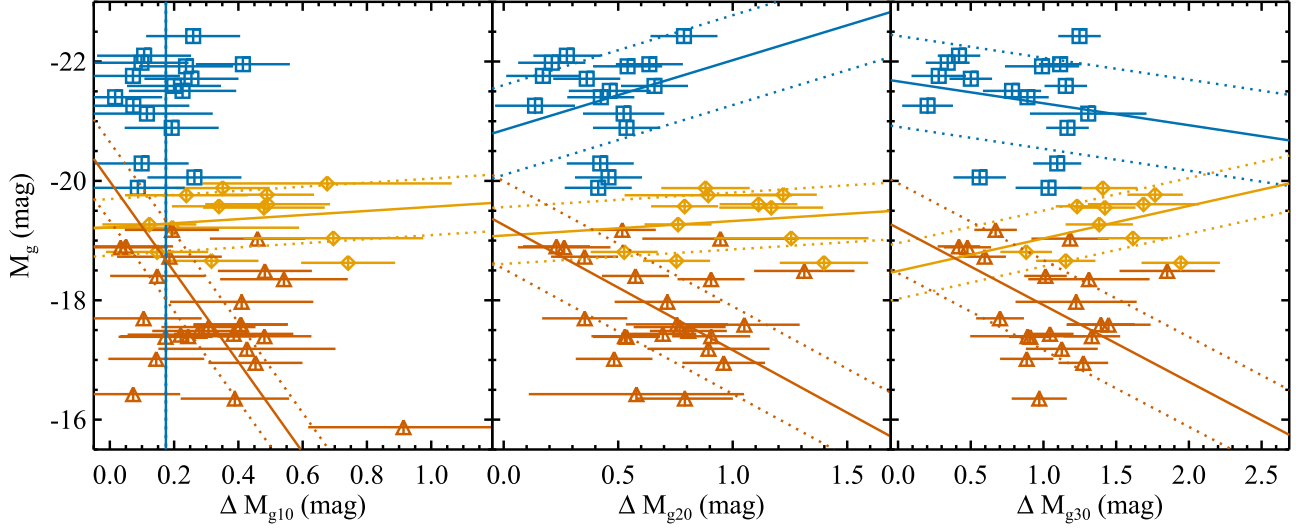


Figure 16. Rest-frame g magnitude at peak and its decay from the peak after 10 (left), 20 (middle), and 30 days (right panel). Blue squares show SLSNe-I, gold diamonds show SNe Ic-BL, and orange triangles SNe Ic, all from PTF. The solid and dotted lines show linear fits through the data and the intrinsic scatter, respectively.

5.9. Cosmology Tests

Because SLSNe can be observed out to large distances, as far out to $z \sim 4$ (Cooke et al. 2012) and likely well beyond with future facilities, the prospects of using SLSNe for cosmological distance determinations is of primary interest. Indeed, Inserra & Smartt (2014) suggested that SLSNe-I may be standardizable, based on (i) the narrowness of the peak magnitude distribution, (ii) a weak correlation between the peak magnitude (at rest-frame 400 nm) and its decay after a certain time, and (iii) the dependence of the peak magnitude (at rest-frame 400 nm) on the SLSN-I color (rest-frame 400–520 nm). We test similar correlations in the current sample.

(i) We use the rest-frame g band as a proxy for the rest-frame 400 nm band of Inserra & Smartt (2014). The peak magnitudes of the SLSNe in our sample are widely distributed around their mean value ($\langle M_g \rangle = -21.14$ mag), with a standard deviation of 0.75 mag, which is almost twice as in the sample of Inserra & Smartt (2014).

(ii) Figure 16 shows the distribution of the rest-frame g peak magnitude, $M_{g,\text{peak}}$, with its decay, ΔM_g , at 10, 20, and 30 days after the peak. These were all calculated from the smoothed light curves (Section 4.3) and can therefore be slightly different from the $M_{g,\text{peak}}$ calculated with the second-order polynomial around the peak (Section 4.1). As a comparison, SLSNe-I and also Type Ic and Ic-BL SNe from PTF are shown in Figure 16. There are very weak correlations, highlighted by the linear fits to the data. However, none of these trends are significant correlations. In every case, the Pearson correlation coefficient is $|r| < 0.3$, and the intrinsic scatter is up to ~ 0.8 mag for SLSNe-I; see Figure 16. The intrinsic scatter of the correlation is the scatter required for the correlation to have $\chi^2 \sim 1$ (Bedregal et al. 2006; Williams et al. 2010), and it is a way of discriminating the observational scatter from what is intrinsic to the correlation. The data and fit results for SLSNe-I are reported in Tables 5 and 6, respectively.

(iii) In Figure 17 and Table 7, we compare the rest-frame g peak magnitude with the rest-frame $g - r$ color at peak. The rest-frame r was derived from the observed i -band photometry using the same techniques as described for the r to rest-frame g conversion. The k -correction values are listed in Table 10. Both

Table 5
Rest-frame g Magnitude at Peak and Its Decay from the Peak after 10, 20, and 30 days, Calculated from the Smoothed Light Curves (Section 4.3)

PTF ID	$M_{g,\text{peak}}$	ΔM_{g10}	ΔM_{g20}	ΔM_{g30}
09atu	-21.8 ± 0.1	0.1 ± 0.1	0.2 ± 0.2	0.3 ± 0.2
09cnd	-22.1 ± 0.1	0.1 ± 0.1	0.3 ± 0.1	0.4 ± 0.1
09cwl	-22.0 ± 0.1	0.1 ± 0.1	0.2 ± 0.1	0.3 ± 0.2
10aacg	-20.1 ± 0.1	0.7 ± 0.5	1.2 ± 0.5	2.0 ± 0.6
10cwr	-21.6 ± 0.1	0.2 ± 0.1	0.7 ± 0.1	1.2 ± 0.1
10hgi	-20.3 ± 0.1	0.1 ± 0.1	0.4 ± 0.1	1.1 ± 0.2
10vqv	-21.5 ± 0.1	0.2 ± 0.2	0.5 ± 0.2	0.8 ± 0.2
10vwg	-21.9 ± 0.1	0.2 ± 0.1	0.5 ± 0.2	1.0 ± 0.3
11dij	-21.4 ± 0.1	0.0 ± 0.1	0.4 ± 0.1	0.9 ± 0.1
11rks	-20.9 ± 0.1	0.2 ± 0.1	0.5 ± 0.1	1.2 ± 0.1
12dam	-21.7 ± 0.1	0.3 ± 0.1	0.4 ± 0.1	0.5 ± 0.1
12gtv	-20.1 ± 0.1	0.3 ± 0.1	0.5 ± 0.1	0.6 ± 0.2
12hni	-19.9 ± 0.1	0.1 ± 0.1	0.4 ± 0.1	1.0 ± 0.2
13ajg	-22.4 ± 0.1	0.3 ± 0.1	0.8 ± 0.1	1.2 ± 0.1
13cjg	-21.1 ± 0.1	0.1 ± 0.2	0.5 ± 0.2	1.3 ± 0.4
13dcc	-22.0 ± 0.1	0.4 ± 0.1	0.6 ± 0.1	1.1 ± 0.1
13ehe	-21.3 ± 0.1	0.1 ± 0.2	0.1 ± 0.2	0.2 ± 0.2

the rest-frame g - and r -band peaks were estimated by fitting a second-order polynomial to the data around peak. We could then constrain the rest-frame $g - r$ for a subsample of SLSNe-I, as listed in Table 7.

The correlation $M_{g,\text{peak}} = A + B \times (g - r)_{\text{peak}}$ is weak, with a Pearson correlation coefficient of 0.59 (null probability $p_r = 0.04$) and a Spearman correlation coefficient of 0.57 (null probability $p_\rho = 0.04$). The normalization and slope are $A = -19.5 \pm 1.2$ and $B = 7.5 \pm 3.8$. In this case, the intrinsic scatter is consistent with zero. While this may suggest a potentially real correlation, it may simply be the consequence of the large error bars that we measure for $g - r$. A larger statistical sample is needed to further investigate the solidity of this relation.

The possible dust reddening $E(B - V)$ of the SLSN-I host galaxies is not taken into account here. While we expect the reddening to be small (e.g., Perley et al. 2016), there may be regions that are locally more dusty (e.g., Cikota et al. 2017).

Table 6
Fit Parameters of the $M_{g,\text{peak}} = A + B \times \Delta M_g$ Relation for SLSNe at Different Epochs (Days after Peak, see Figure 16 and Table 5)

t	A	B	σ_{int}	r	p_r	ρ	p_ρ
10	-0.24	0.37	-0.23	0.39
20	-20.9 ± 0.5	-1.2 ± 1.1	0.75	-0.10	0.71	-0.11	0.69
30	-21.7 ± 0.5	0.4 ± 0.5	0.76	0.14	0.60	0.15	0.57

Note. σ_{int} is the intrinsic scatter (see text). r and ρ are the Pearson and Spearman correlation coefficients, respectively, and are listed with their respective null probability (p_r and p_ρ).

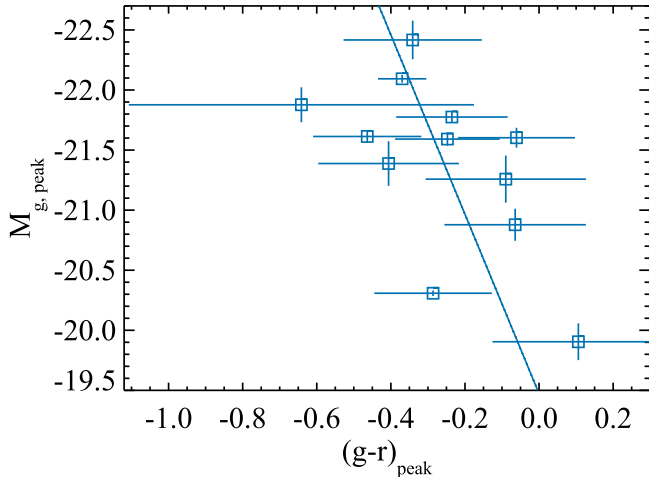


Figure 17. Rest-frame g peak magnitude vs. the rest-frame $g - r$ color at peak, for PTF SLSNe. The solid line shows a linear fit to the data. The Pearson correlation coefficient is $r = 0.6$.

Table 7
Rest-frame g and Rest-frame $g - r$ Magnitudes at Peak for the SLSNe in Our Sample (see Figure 17)

PTF ID	$M_{g,\text{peak}}$	$g - r(\text{peak})$
09atu	-21.78 ± 0.04	-0.24 ± 0.15
09cnd	-22.09 ± 0.03	-0.37 ± 0.07
10cwr	-21.59 ± 0.06	-0.25 ± 0.14
10hgi	-20.31 ± 0.02	-0.29 ± 0.16
11dij	-21.39 ± 0.19	-0.41 ± 0.19
11rks	-20.88 ± 0.13	-0.06 ± 0.19
12dam	-21.61 ± 0.05	-0.46 ± 0.15
12gtv	-19.90 ± 0.15	0.11 ± 0.23
12mxx	-21.60 ± 0.08	-0.06 ± 0.16
13ajg	-22.42 ± 0.16	-0.34 ± 0.19
13dcc	-21.88 ± 0.15	-0.64 ± 0.47
13ehe	-21.26 ± 0.20	-0.09 ± 0.22

However, a case-to-case characterization of the host-galaxies' $E(B - V)$ is not possible here and is beyond the scope of this paper.

While we find the same overall trends as Inserra & Smartt (2014), the diagnostics above show mostly weaker correlations than reported by their work. One exception is the relation between the peak magnitude and $g - r$ at peak, for which we find a similar Pearson correlation coefficient to Inserra & Smartt (2014).

We further investigate possible correlations of M_g with other variables, such as the early decay slope or host metallicity, with

no convincing results. The weak trends of M_g with the rise and decay times are shown in Figure 6. We therefore cannot strengthen the claim that SLSNe might be standardizable candles with the current data. Future transient surveys may clarify this issue with much improved statistics (e.g., Scovacricchi et al. 2016).

6. Conclusions

We study a sample of 26 SLSNe-I, all discovered by the PTF survey with light-curve coverage out to late times, well beyond 100 days after peak for half of the sample. Based on our analysis, we conclude the following.

1. The absolute peak magnitudes of PTF spectroscopically classified SLSNe-I are $-22.5 \lesssim M_g \lesssim -20$ mag (Sections 4.1 and 5.1). The mean SLSN-I peak magnitude is -21.14 mag, which is brighter than the mean magnitudes of SNe Ic-BL and SNe Ib/c by about 2 and 4 mag, respectively. When including volumetric corrections, the peak-magnitude distribution evolves smoothly from SNe Ib/c to SNe Ic-BL, and to SLSNe-I. There is only very little overlap between the faintest SLSNe-I and the brightest SNe Ic-BL.
2. At early times (< 60 days after peak) SLSNe-I tend to decay faster (0.04 mag day $^{-1}$ on average) and with a wider range of decay rates than at late times (> 60 days); see Sections 4.2 and 5.3.
3. At late times, all SLSN-I light curves for which sufficient data are available cluster around the decay rate of ~ 1 mag per 100 days, which is consistent with the radioactive decay of ^{56}Co to stable ^{56}Fe (Sections 4.2 and 5.3).
4. We observe no gap between fast- and slow-declining SLSNe-I. Nevertheless, virtually all slow-declining events (SLSN-R) show early- and late-time bumps/plateau which are not as common in classical SLSNe-I. Thus, the possibility is still that SLSN-I/R represent a subclass of SLSN-I (Sections 4.2 and 5.3).
5. SLSNe-I rise more slowly than SNe Ib/c and Ic-BL (i.e., SLSNe have longer rise timescales $t_{\text{rise}}^{\Delta 1 \text{ mag}}$ by roughly 10 days), even for similar decay times. Indeed, the rise times correlate differently with the decay times for SLSNe-I and SNe Ib/c (Sections 4.4, 4.5, and 5.4).
6. This implies that the light curves of SLSNe-I are different from SNe Ib/c and Ic-BL, and therefore SLSNe-I can be considered as a separate population photometrically, as well as spectroscopically.
7. The peaks of SLSNe-I are not powered by the production of radioactive nickel, unless there are strong asymmetries in the ejecta (Section 5.6).

8. Late-time light curves can be explained with the radioactive decay of Ni masses ranging from 1 to $10 M_{\odot}$. Radioactive decay might be an important powering source at these stages (Section 5.6).
9. The slope of the late-time decay is in a few SLSNe-I faster than the radioactive decay. This can be explained by the escape of γ -rays from the massive ejecta. Our simulations of the radiative decay energy deposition for massive progenitors shows that the trapping is reduced for higher expansion velocities and higher Ni fractions of the ejected masses (Section 5.7).
10. The majority of the SLSN-I light curves can reasonably well be reproduced also with a spinning-down magnetar model, with the exceptions of PTF 10hgi, PTF 10vvg, PTF 11dij, and PTF 11rks (Section 5.8). The derived magnetic fields lie in the parameter space where a magnetar model can mimic the radioactive decay of ^{56}Co .
11. We cannot distinguish between a radioactively powered and magnetar light curves at this stage. Very late-time observations are needed to disentangle between the magnetar and radioactive models.
12. We find no correlation between the magnetar spin and the host metallicity (Section 5.8).
13. We find similar correlations to those claimed to make SLSN-I standardizable candles (Inserra & Smartt 2014); see Section 5.9. These correlations are significantly weaker, except for the correlation between the rest-frame g -band peak magnitude with the rest-frame $g - r$ at peak. With the current data, we cannot strengthen the potential of exploiting SLSNe for cosmology.

We thank the referee for a useful and constructive report, which helped make the paper more robust. We thank L. Dessart, A. Jerkstrand, A. Kozyreva, and the SLSN MIAPP 2017 workshop participants for insightful discussions. A.D.C. acknowledges support by the Weizmann Institute of Science Koshland Center for Basic Research. Support for I.A. was provided by NASA through the Einstein Fellowship Program, grant PF6-170148. M.S. acknowledges support from EU/FP7-ERC grant No. [615929]. K.M. acknowledges support from the STFC through an Ernest Rutherford Fellowship. E.O.O. is grateful for support by grants from the Israel Science Foundation, Minerva, Israeli ministry of Science, the US-Israel Binational Science Foundation and the I-CORE Program of the Planning and Budgeting Committee and The Israel Science Foundation. A.C. acknowledges support from the NSF CAREER award 1455090. M.M.K. acknowledges support from the GROWTH project funded by the National Science Foundation under grant No. 1545949. The intermediate Palomar Transient Factory project is a scientific collaboration among the California Institute of Technology, Los Alamos

National Laboratory, the University of Wisconsin, Milwaukee, the Oskar Klein Center, the Weizmann Institute of Science, the TANGO Program of the University System of Taiwan, and the Kavli Institute for the Physics and Mathematics of the Universe. LANL participation in iPTF is supported by the US Department of Energy as a part of the Laboratory Directed Research and Development program. A portion of this work was carried out at the Jet Propulsion Laboratory under a Research and Technology Development Grant, under contract with the National Aeronautics and Space Administration. This research has made use of the NASA/IPAC Infrared Science Archive, which is operated by the Jet Propulsion Laboratory, California Institute of Technology, under contract with the National Aeronautics and Space Administration. This research has made use of NASA’s Astrophysics Data System. This paper made use of Lowell Observatory’s Discovery Channel Telescope (DCT). Lowell operates the DCT in partnership with Boston University, Northern Arizona University, the University of Maryland, and the University of Toledo. Partial support of the DCT was provided by Discovery Communications. Large Monolithic Imager (LMI) on DCT was built by Lowell Observatory using funds from the National Science Foundation (AST-1005313). This work makes use of observations taken with the LCO network. This research has made use of the NASA/IPAC Extragalactic Database (NED) which is operated by the Jet Propulsion Laboratory, California Institute of Technology, under contract with the National Aeronautics and Space Administration. Some of the data presented herein were obtained at the W.M. Keck Observatory, which is operated as a scientific partnership among the California Institute of Technology, the University of California and the National Aeronautics and Space Administration. The Observatory was made possible by the generous financial support of the W.M. Keck Foundation. The authors wish to recognize and acknowledge the very significant cultural role and reverence that the summit of Maunakea has always had within the indigenous Hawaiian community. We are most fortunate to have the opportunity to conduct observations from this mountain.

Software: MS pipeline (Sullivan et al. 2006; Ofek et al. 2014a; Firth et al. 2015; Dimitriadis et al. 2017), LPIPE (<http://www.astro.caltech.edu/~dperley/programs/lpipe.html>), LCOGT pipeline (Valenti et al. 2016), HOTPANTS (<http://www.astro.washington.edu/users/becker/v2.0/hotpants.html>), IRAF (Tody 1986, 1993), SWarp (Bertin et al. 2002), DrizzlePac 2.0 (<http://drizzlepac.stsci.edu>).

Appendix A SLSN-I Light-curve Properties

The light-curve properties of the (i) PTF SLSN-I sample that we derived above (i.e., peak magnitude, early- and late-time decay, and rise and decay timescales) are reported in Table 8.

Table 8
Light-curve Properties of the H-poor SLSN Sample

PTF ID	MJD _{peak}	$M_{g,\text{peak}}$ (mag)	$\chi^2_{\nu,\text{peak}}/\nu$	Slope1 ^a (mag day ⁻¹)	$\chi^2_{\nu,\text{Slope1}}/\nu$	Slope2 ^a (mag day ⁻¹)	$\chi^2_{\nu,\text{Slope2}}/\nu$	Int ^b (days)	t_{rise}^1 mag (days)	t_{fall}^1 mag (days)	$t_{\text{rise},1/2}$ (days)	$t_{\text{fall},1/2}$ (days)
22	09as	54918.20	(−19.51 ± 0.13)	0.30/8	0.0830 ± 0.0121	0.27/9	11 ± 3	...	9 ± 3
	09atu	55062.32	−21.78 ± 0.04	0.20/22	0.0137 ± 0.0052	0.27/13	37 ± 2	70 ± 8	32 ± 3	61 ± 11
	09cnd	55086.35	−22.09 ± 0.03	0.17/28	0.0226 ± 0.0018	0.61/8	33 ± 2	54 ± 6	29 ± 2	45 ± 4
	09cwl	55067.25	−22.03 ± 0.13	0.44/3	0.0320 ± 0.0012	0.98/2	25 ± 2	...	21 ± 2	54 ± 7
	10aagc	55499.48	−20.12 ± 0.25	1.69/28	0.0745 ± 0.0042	1.16/26	17 ± 9	...	11 ± 5
	10bfz	55227.46	(−20.86 ± 0.03)	0.15/5	0.0658 ± 0.0026	0.85/30	33 ± 4	...	28 ± 2
	10bjp	55252.52	−20.52 ± 0.16	0.41/9	0.0241 ± 0.0154	1.73/4	42 ± 2
	10cwr	55281.23	−21.59 ± 0.06	0.46/10	0.0675 ± 0.0038	3.76/2	28 ± 2	...	23 ± 2
	10hgi	55367.43	−20.31 ± 0.02	0.09/22	0.0519 ± 0.0033	0.92/12	0.0211 ± 0.0011	0.93/12	37.7	32 ± 2	28 ± 2	29 ± 2
	10nmn	55384.20	−20.53 ± 0.04	0.02/2	0.0080 ± 0.0003	0.26/16	...	61 ± 18
	10uhf	55452.25	−20.60 ± 0.22	1.50/12	0.0356 ± 0.0072	1.48/6
	10vqv	55470.52	−21.58 ± 0.11	0.40/14	0.0338 ± 0.0043	0.12/6	0.0186 ± 0.0084	0.27/5	55.6	...	36 ± 5	...
	10vwg	55455.29	−21.94 ± 0.20	2.89/19	0.0451 ± 0.0019	9.48/8	0.0119 ± 0.0029	0.67/5	43.0	39 ± 2	...	33 ± 3
	11dij	55684.37	−21.39 ± 0.19	5.44/22	0.0550 ± 0.0005	4.92/30	0.0141 ± 0.0018	0.26/3	74.5	15 ± 2	31 ± 2	13 ± 2
	11hrq	55753.48	(−19.80 ± 0.04)	0.32/23	0.0156 ± 0.0006	0.45/45	0.0163 ± 0.0006	1.25/58	7.4	...	55 ± 6	...
	11rks	55935.14	−20.88 ± 0.13	1.84/50	0.0501 ± 0.0021	1.62/30	0.0085 ± 0.0072	1.39/2	60.0	17 ± 2	27 ± 2	15 ± 2
	12dam	56092.33	−21.61 ± 0.05	4.72/45	0.0137 ± 0.0002	4.84/17	0.0178 ± 0.0002	5.35/52	113.4	34 ± 2	62 ± 5	29 ± 2
	12gty	56143.36	−19.90 ± 0.15	0.80/20	0.0277 ± 0.0031	2.41/9	0.0115 ± 0.0028	0.88/7	54.9	36 ± 3	41 ± 11	28 ± 3
	12hni	56154.25	−19.92 ± 0.10	1.78/11	0.0470 ± 0.0016	1.21/11	−0.0217 ± 0.0071	0.52/4	74.1	...	29 ± 4	...
	12mxx	56292.14	−21.60 ± 0.08	0.93/30	29 ± 2	...	26 ± 2	...
	13ajg	56410.35	−22.42 ± 0.16	1.00/69	0.0376 ± 0.0033	1.86/50	0.0096 ± 0.0008	10.32/1	87.6	24 ± 2	25 ± 2	21 ± 2
	13bdl	56493.22	−20.36 ± 0.22	0.66/28
	13bjz	56438.17	−20.81 ± 0.18	2.53/15	8 ± 2	...
	13cjq	56506.28	−21.13 ± 0.09	0.66/45	0.0409 ± 0.0056	2.71/7	0.0046 ± 0.0052	0.79/2	49.3	...	25 ± 5	...
	13dcc	56612.35	−21.88 ± 0.15	0.59/49	0.0476 ± 0.0044	1.96/15	0.0122 ± 0.0007	0.88/3	62.3	...	28 ± 2	...
	13ehe	56669.54	−21.26 ± 0.20	0.92/31	0.0062 ± 0.0065	1.29/4	0.0158 ± 0.0007	0.14/1	37.9	...	114 ± 7	...
												97 ± 10

Note. SLSNe with best sampled data, where the light curves can be fully characterized in their rise and fall times, peaks, early- and late-time declines, are highlighted in bold. Peak magnitudes are in parenthesis for the cases where the peak is not sufficiently covered, so these represent magnitude upper limits. The peak magnitude for PTF 10nmn is taken from O. Yaron et al. (2018, in preparation), which includes a more complete coverage of the peak. In the case of PTF 12hni the late-time decay slope is negative because of the light curve rebrightening. The χ^2_ν are sometimes large because the formal errors in the observed magnitudes within the fitted time interval are very small (e.g., between 0.006 and 0.024 mag around peak for PTF 12dam).

^a Slopes of the postpeak early- and late-time linear fit to the data (Section 4.2).

^b Intersection between the postpeak early- and late-times linear fits to the data (in days after peak, Section 4.2).

Appendix B

Appendix Figures

Figures 18–22 below show the light curves of (i) PTF SLSNe-I in our sample, their rise and decay timescales in flux and magnitudes, the magnetar fits to the data, and their confidence levels.

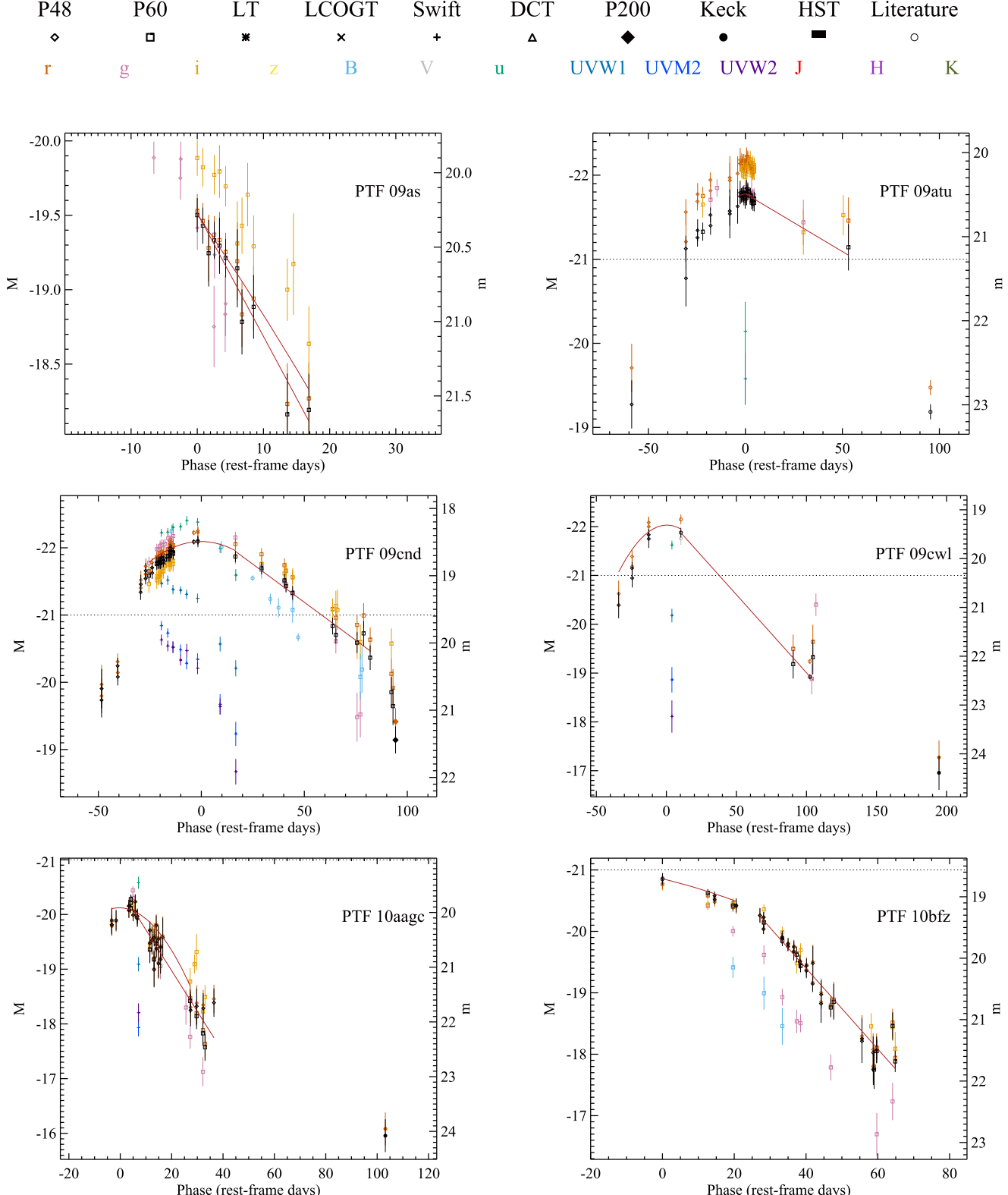


Figure 18. Light curves of (i)PTF SLSNe-I in our sample for individual observed filters and rest-frame M_g (black). Both apparent and absolute magnitudes are corrected for Galactic foreground dust extinction (see Section 3.12). The solid lines show the second-order polynomial fit around peak (Section 4.1) and the postpeak- and late-time decay linear fits to the data (Section 4.2). The horizontal dotted line marks the $M = -21$ mag “historical” threshold for SLSNe, for comparison.

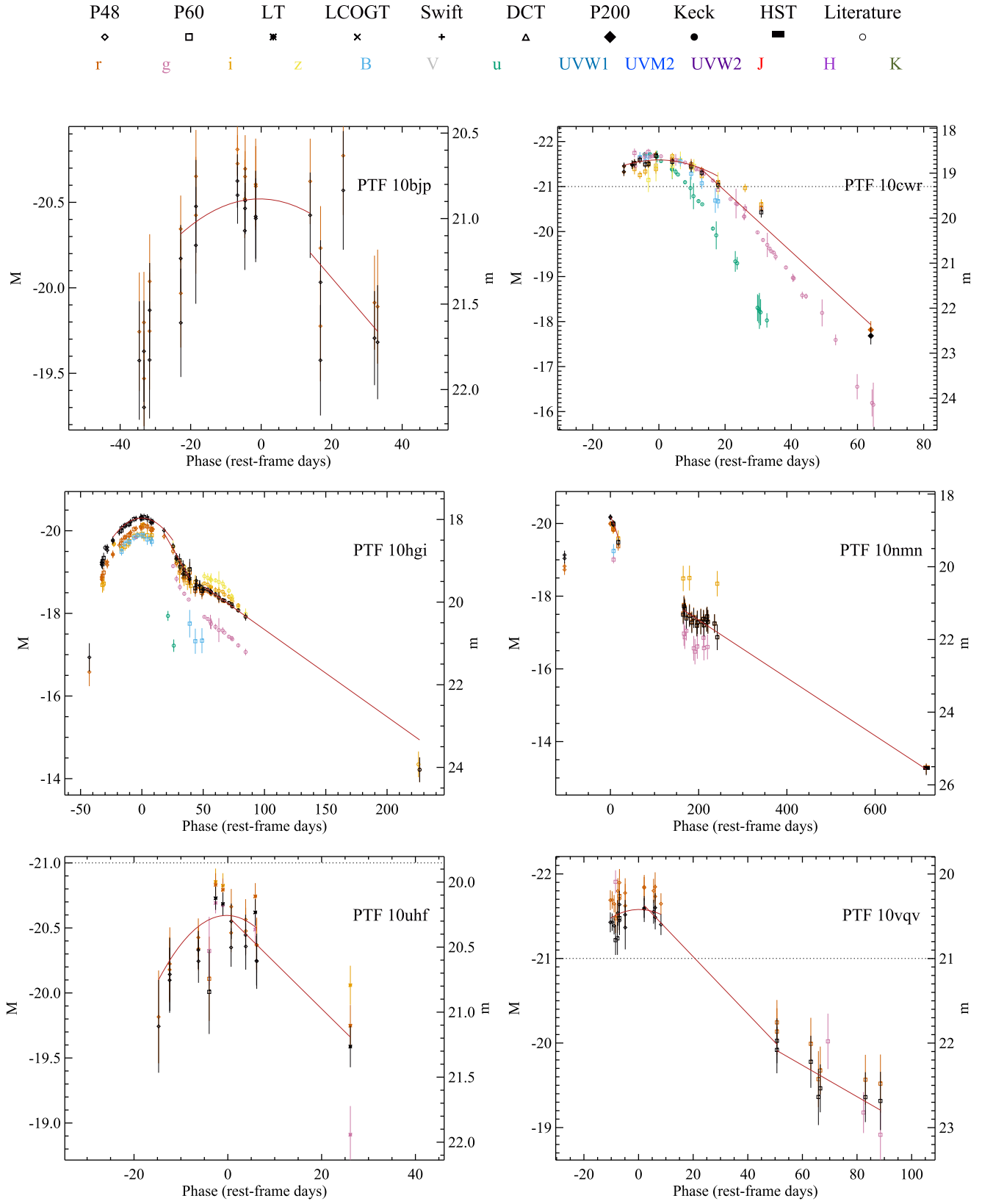


Figure 18. (Continued.)

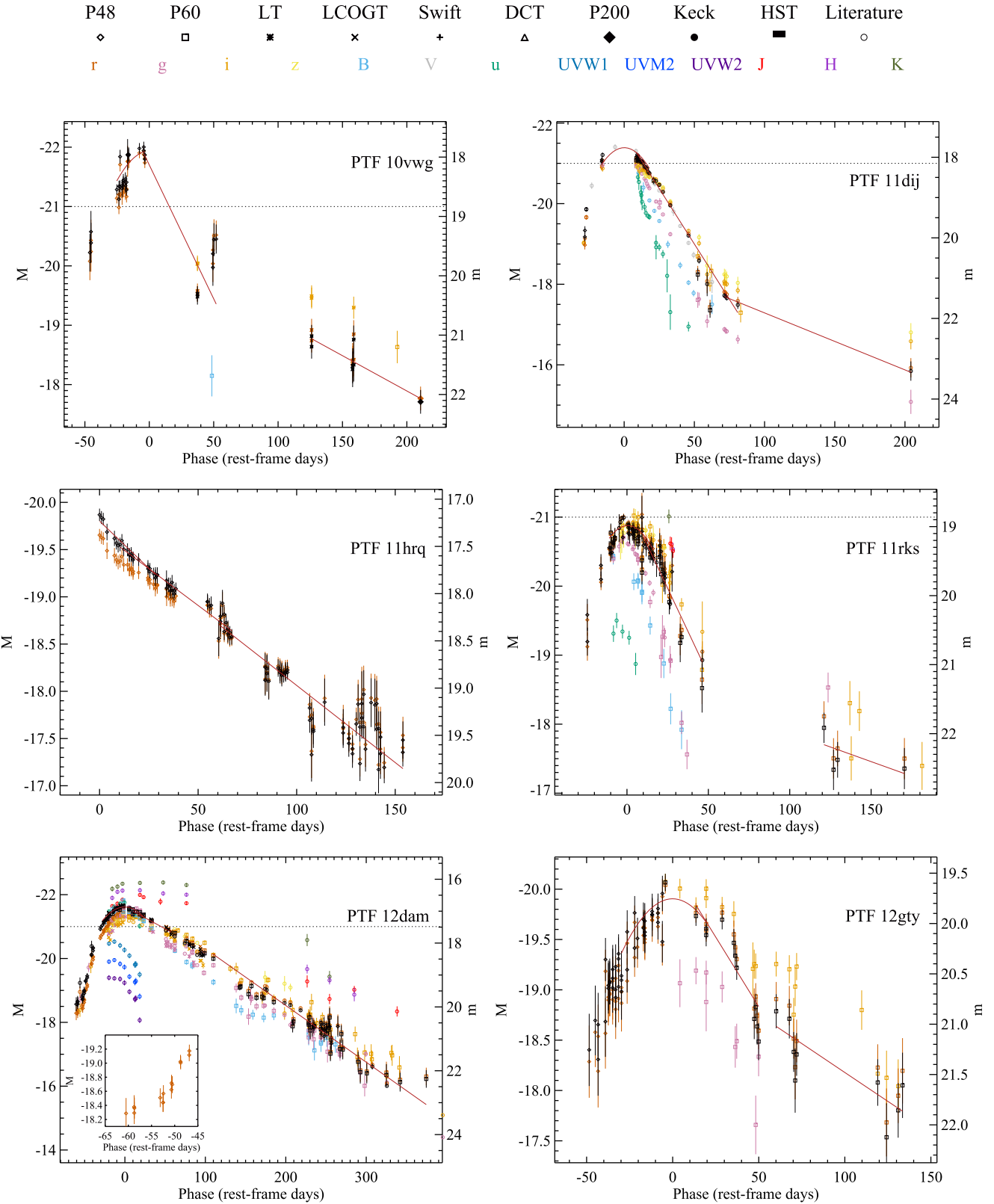
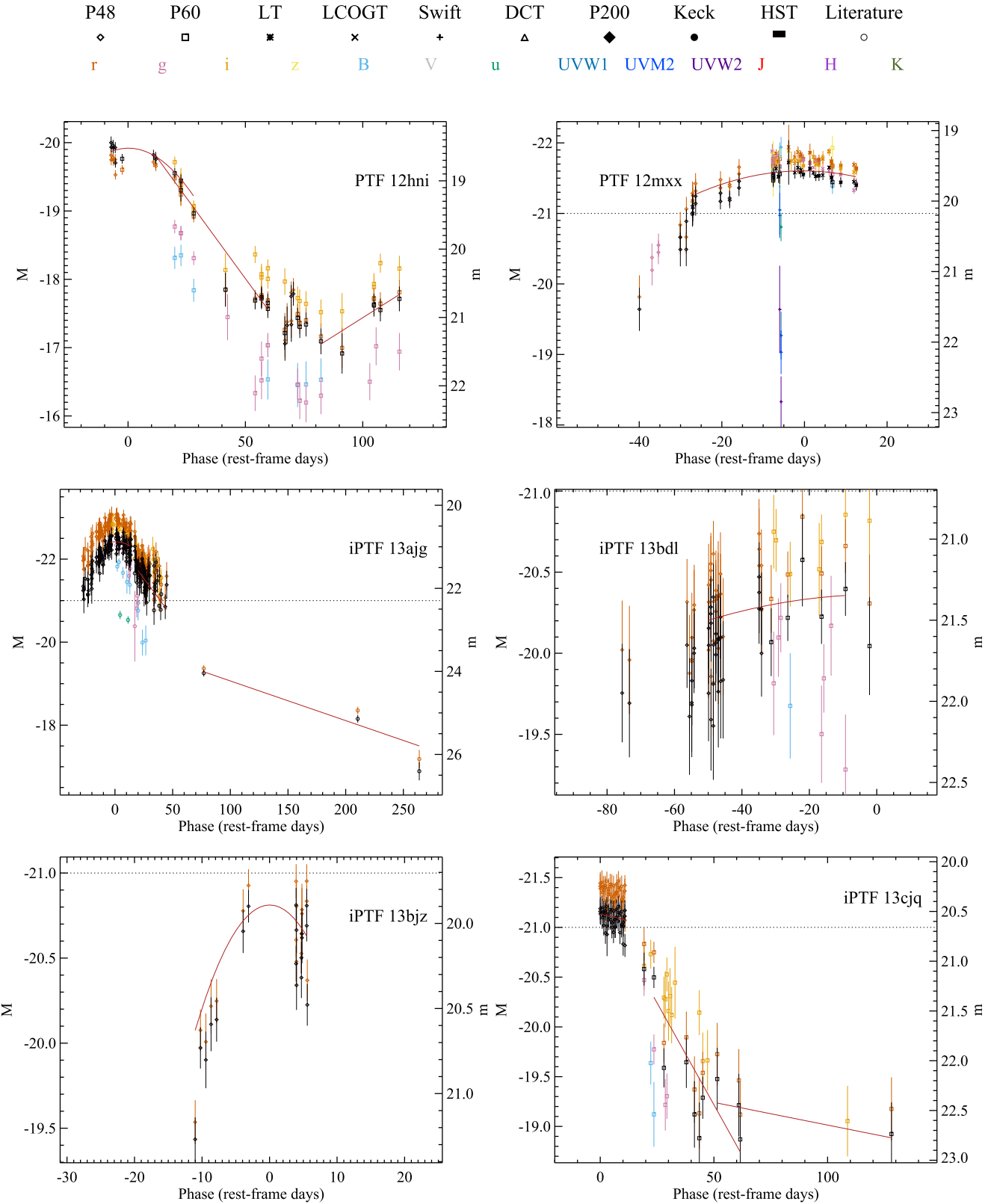


Figure 18. (Continued.)

**Figure 18.** (Continued.)

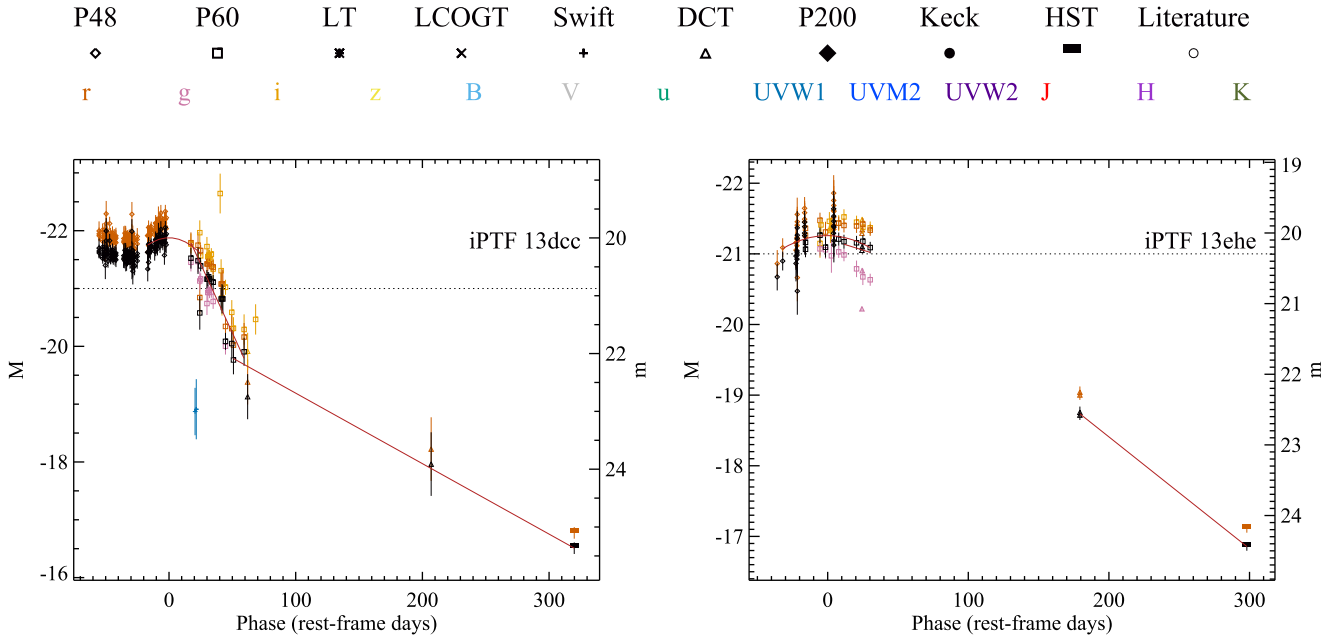


Figure 18. (Continued.)

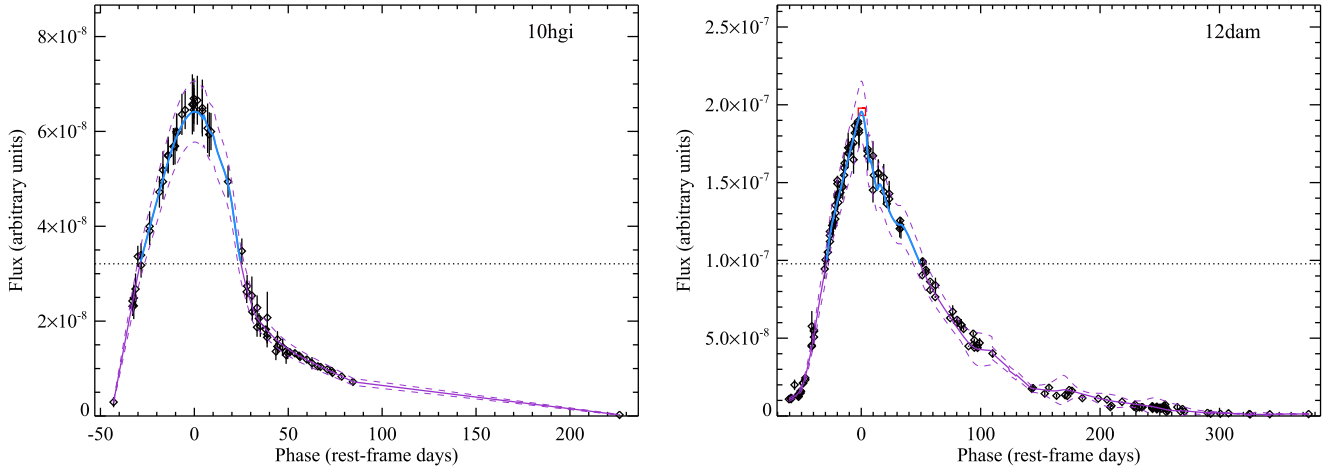


Figure 19. The rest-frame g -band light curves of two SLSNe-I in flux (black diamonds). The smoothed light curves (described in Section 4.3) are shown by the solid curves. The red squares indicate the auxiliary points introduced for the light-curve smoothing. The horizontal dotted line marks the half-flux limit, which is used to calculate the $t_{\text{rise},1/2}$ and $t_{\text{fall},1/2}$ timescales (Section 5.4), when the light curve is well-characterized between the half-flux limit and the peak (highlighted blue solid curves). (The complete figure set (26 images) is available.)

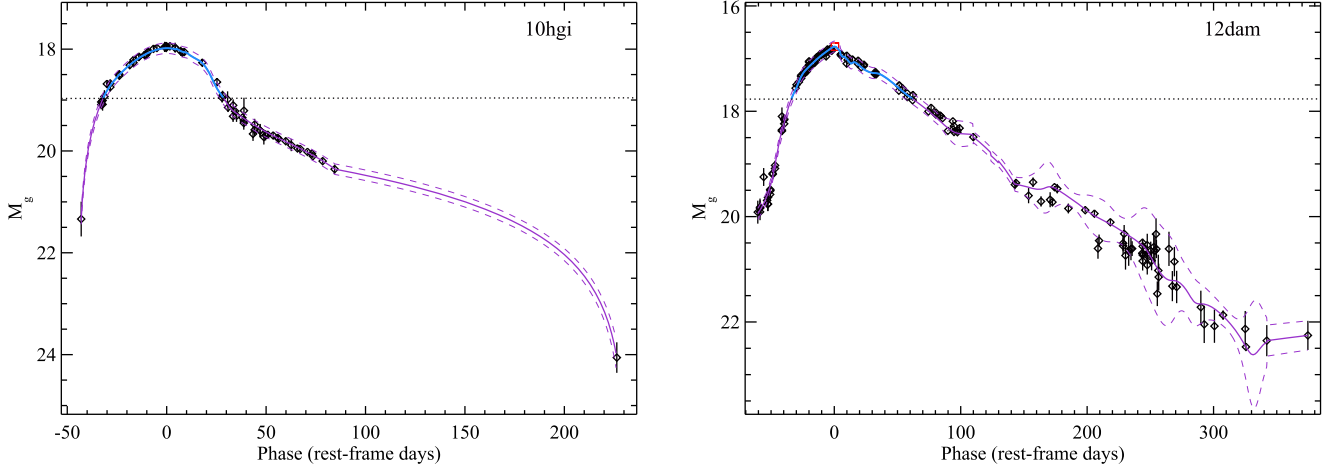


Figure 20. Same as Figure 19, but for magnitudes. The horizontal dotted lines mark here the distance of 1 mag from peak, which is used to calculate the $t_{\text{rise}}^{\Delta 1 \text{ mag}}$ and $t_{\text{fall}}^{\Delta 1 \text{ mag}}$ timescales, when the light curves are well-characterized above this threshold (highlighted blue solid curves).

(The complete figure set (26 images) is available.)

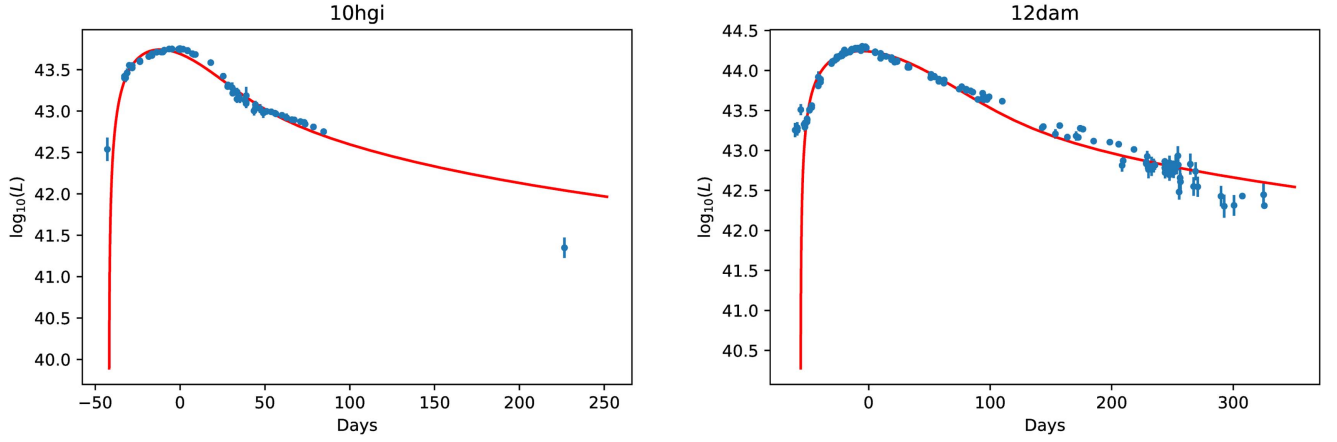
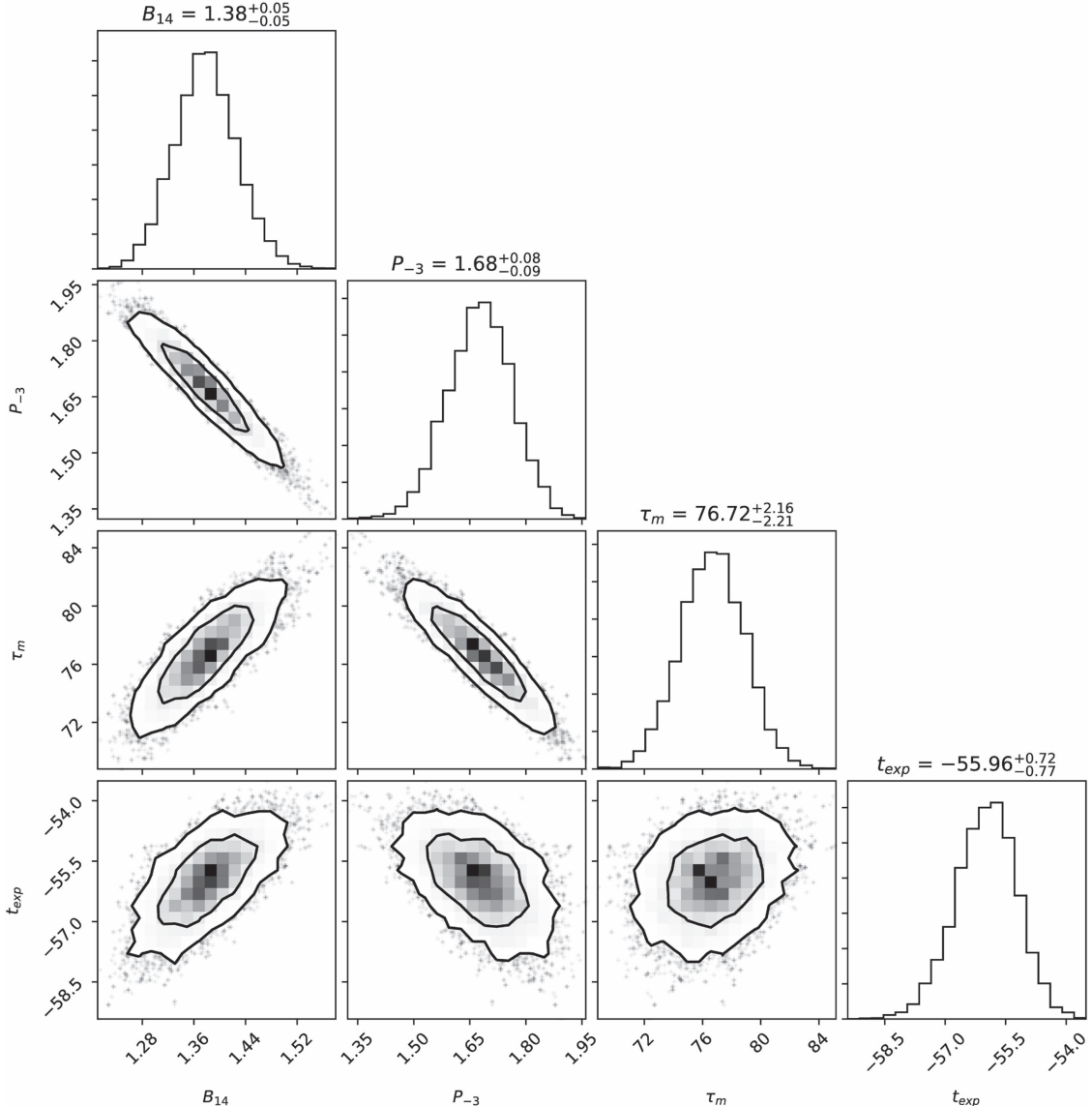


Figure 21. Magnetar fit to the bolometric light curves.

(The complete figure set (14 images) is available.)

**Figure 22.** Confidence levels of the best-fit parameters for the magnetar model of PTF 12dam.

(The complete figure set (14 images) is available.)

Appendix C *k*-correction Tables

The *k*-corrections from *r* to rest-frame *g* (K_{gr}) and from *i* to rest-frame *r* (K_{ir}) for the (i) PTF SLSN sample are listed in Tables 9 and 10 below.

Appendix D Photometric Data

All magnitudes are in the AB system. The absolute magnitudes in rest-frame *g*-band are derived from $M_g = m_r - DM - K_{gr}$, where DM is the distance modulus,

Table 9
 K_{gr} Corrections

PTF ID z	09as 0.1864	09atu 0.5014	09cnd 0.2585	09cwl 0.3502	10aagc 0.2067	10bfz 0.1699	10bjp 0.3585	10cwr 0.2301	10hgi 0.0982	10nmn 0.1236	10uhf 0.2879	10vqv 0.4520	10vwg 0.1901
phase	K_{gr}												
-25	0.00	-0.50	-0.13	-0.30	-0.04	0.04	-0.31	-0.08	0.20	0.16	-0.19	-0.42	-0.01
-24	-0.00	-0.50	-0.14	-0.30	-0.04	0.04	-0.32	-0.09	0.20	0.15	-0.19	-0.42	-0.01
-23	-0.00	-0.49	-0.14	-0.30	-0.05	0.03	-0.32	-0.09	0.19	0.15	-0.19	-0.42	-0.01
-22	-0.01	-0.49	-0.14	-0.30	-0.05	0.03	-0.32	-0.09	0.19	0.14	-0.20	-0.42	-0.02
-22	-0.01	-0.49	-0.14	-0.31	-0.05	0.03	-0.32	-0.10	0.18	0.14	-0.20	-0.42	-0.02

(This table is available in its entirety in machine-readable form.)

Table 10
 K_{ri} Corrections

PTF ID z	09as 0.1864	09atu 0.5014	09cnd 0.2585	09cwl 0.3502	10aagc 0.2067	10bfz 0.1699	10bjp 0.3585	10cwr 0.2301	10hgi 0.0982	10nmn 0.1236	10uhf 0.2879	10vqv 0.4520	10vwg 0.1901
phase	K_{ri}												
-25	-0.16	-0.70	-0.26	-0.44	-0.20	-0.13	-0.46	-0.23	-0.05	-0.08	-0.30	-0.62	-0.17
-24	-0.16	-0.70	-0.26	-0.44	-0.20	-0.13	-0.46	-0.23	-0.05	-0.08	-0.30	-0.61	-0.17
-23	-0.16	-0.70	-0.26	-0.44	-0.20	-0.13	-0.46	-0.23	-0.06	-0.08	-0.30	-0.61	-0.17
-22	-0.16	-0.69	-0.26	-0.44	-0.20	-0.13	-0.46	-0.23	-0.06	-0.08	-0.30	-0.61	-0.17
-22	-0.16	-0.69	-0.26	-0.44	-0.20	-0.13	-0.46	-0.23	-0.06	-0.09	-0.30	-0.61	-0.17

(This table is available in its entirety in machine-readable form.)

Table 11
PTF 09as Photometry Data

MJD	Phase	m	Filter	Telescope
54910.417	-6.56	19.71 ± 0.11	<i>g</i>	p48
54915.164	-2.56	19.85 ± 0.14	<i>g</i>	p48
54915.244	-2.49	19.72 ± 0.12	<i>g</i>	p48
54918.197	0.00	20.13 ± 0.11	<i>r</i>	p60
54918.199	0.00	19.80 ± 0.12	<i>i</i>	p60
54918.210	0.01	20.19 ± 0.15	<i>g</i>	p48
54919.195	0.84	20.19 ± 0.12	<i>r</i>	p60
54919.197	0.84	19.86 ± 0.13	<i>i</i>	p60
54920.235	1.72	20.38 ± 0.22	<i>r</i>	p60
54921.206	2.54	20.85 ± 0.27	<i>g</i>	p48
54921.248	2.57	20.29 ± 0.13	<i>r</i>	p60
54921.249	2.57	19.91 ± 0.13	<i>i</i>	p60
54921.294	2.61	20.37 ± 0.16	<i>g</i>	p48
54922.186	3.36	20.32 ± 0.19	<i>r</i>	p60
54922.187	3.36	19.89 ± 0.18	<i>i</i>	p60
54923.199	4.22	20.77 ± 0.25	<i>g</i>	p48
54923.283	4.29	20.40 ± 0.13	<i>r</i>	p60
54923.285	4.29	19.99 ± 0.14	<i>i</i>	p60
54923.286	4.29	20.70 ± 0.22	<i>g</i>	p48
54925.376	6.05	20.47 ± 0.26	<i>r</i>	p60
54925.377	6.05	20.37 ± 0.28	<i>i</i>	p60
54926.214	6.76	20.82 ± 0.22	<i>r</i>	p60
54926.215	6.76	20.25 ± 0.19	<i>i</i>	p60
54927.223	7.61	20.04 ± 0.21	<i>i</i>	p60
54928.297	8.51	20.72 ± 0.22	<i>r</i>	p60
54928.299	8.52	20.39 ± 0.21	<i>i</i>	p60
54934.333	13.60	21.42 ± 0.27	<i>r</i>	p60
54934.335	13.60	20.68 ± 0.21	<i>i</i>	p60
54935.427	14.52	20.51 ± 0.34	<i>i</i>	p60
54938.202	16.86	21.39 ± 0.24	<i>r</i>	p60
54938.204	16.87	21.05 ± 0.25	<i>i</i>	p60

(This table is available in its entirety in machine-readable form.)

Table 12
PTF 09as Rest-frame *g* Photometry Data

MJD	Phase	m_g	M_g	Telescope	Reference
54918.197	0.00	20.29 ± 0.11	-19.50	p60	...
54919.195	0.84	20.36 ± 0.12	-19.43	p60	...
54920.235	1.72	20.54 ± 0.22	-19.24	p60	...
54921.248	2.57	20.45 ± 0.13	-19.33	p60	...
54922.186	3.36	20.49 ± 0.19	-19.30	p60	...
54923.283	4.29	20.57 ± 0.13	-19.21	p60	...
54925.376	6.05	20.64 ± 0.26	-19.14	p60	...
54926.214	6.76	21.00 ± 0.22	-18.78	p60	...
54928.297	8.51	20.90 ± 0.22	-18.88	p60	...
54934.333	13.60	21.62 ± 0.27	-18.16	p60	...
54938.202	16.86	21.59 ± 0.24	-18.19	p60	...

(This table is available in its entirety in machine-readable form.)

m_r is corrected for foreground Galactic extinction (Table 1), and K_{gr} is the k -correction (Table 9), as described in Section 3.12. Here we show only the photometric data of PTF 09as as example, in Tables 11 and 12. The complete set of photometric data for all SLSNe are available as machine-readable electronic tables. The UV photometry from *Swift* was not corrected from host-galaxy contribution, but this should be minimal (see Section 3.7). The table references are (I) Quimby et al. (2011); (II) Pastorello et al. (2010); (III) Inserra et al. (2013); (IV) Nicholl et al. (2013); Chen et al. (2015); (V) Vreeswijk et al. (2014).

ORCID iDs

Annalisa De Cia <https://orcid.org/0000-0003-2082-1626>
A. Gal-Yam <https://orcid.org/0000-0002-3653-5598>

- A. Rubin [DOI](https://orcid.org/0000-0003-4557-0632) <https://orcid.org/0000-0003-4557-0632>
 G. Leloudas [DOI](https://orcid.org/0000-0002-8597-0756) <https://orcid.org/0000-0002-8597-0756>
 P. Vreeswijk [DOI](https://orcid.org/0000-0002-7572-9088) <https://orcid.org/0000-0002-7572-9088>
 D. A. Perley [DOI](https://orcid.org/0000-0001-8472-1996) <https://orcid.org/0000-0001-8472-1996>
 R. Quimby [DOI](https://orcid.org/0000-0001-9171-5236) <https://orcid.org/0000-0001-9171-5236>
 Lin Yan [DOI](https://orcid.org/0000-0003-1710-9339) <https://orcid.org/0000-0003-1710-9339>
 M. Sullivan [DOI](https://orcid.org/0000-0001-9053-4820) <https://orcid.org/0000-0001-9053-4820>
 J. Sollerman [DOI](https://orcid.org/0000-0003-1546-6615) <https://orcid.org/0000-0003-1546-6615>
 D. Bersier [DOI](https://orcid.org/0000-0001-7485-3020) <https://orcid.org/0000-0001-7485-3020>
 S. B. Cenko [DOI](https://orcid.org/0000-0003-1673-970X) <https://orcid.org/0000-0003-1673-970X>
 E. O. Ofek [DOI](https://orcid.org/0000-0002-6786-8774) <https://orcid.org/0000-0002-6786-8774>
 J. Spyromilio [DOI](https://orcid.org/0000-0001-6815-4055) <https://orcid.org/0000-0001-6815-4055>
 S. Valenti [DOI](https://orcid.org/0000-0001-8818-0795) <https://orcid.org/0000-0001-8818-0795>
 I. Arcavi [DOI](https://orcid.org/0000-0001-7090-4898) <https://orcid.org/0000-0001-7090-4898>
 A. Corsi [DOI](https://orcid.org/0000-0001-8104-3536) <https://orcid.org/0000-0001-8104-3536>
 D. A. Howell [DOI](https://orcid.org/0000-0003-4253-656X) <https://orcid.org/0000-0003-4253-656X>
 P. Mazzali [DOI](https://orcid.org/0000-0001-6876-8284) <https://orcid.org/0000-0001-6876-8284>
 M. M. Kasliwal [DOI](https://orcid.org/0000-0002-5619-4938) <https://orcid.org/0000-0002-5619-4938>

References

- Abbott, T., Cooke, J., Curtin, C., et al. 2017, *PASA*, **34**, e012
 Ahn, C. P., Alexandroff, R., Allende Prieto, C., et al. 2014, *ApJS*, **211**, 17
 Arcavi, I., Gal-Yam, A., Kasliwal, M. M., et al. 2010, *ApJ*, **721**, 777
 Arnett, W. D. 1979, *ApJL*, **230**, L37
 Arnett, W. D. 1982, *ApJ*, **253**, 785
 Barkat, Z., Rakavy, G., & Sack, N. 1967, *PhRvL*, **18**, 379
 Bazin, G., Ruhlmann-Kleider, V., Palanque-Delabrouille, N., et al. 2011, *A&A*, **534**, A43
 Bedregal, A. G., Aragón-Salamanca, A., & Merrifield, M. R. 2006, *MNRAS*, **373**, 1125
 Bertin, E., Mellier, Y., Radovich, M., et al. 2002, in ASP Conf. Ser. 281, Astronomical Data Analysis Software and Systems XI, ed. D. A. Bohlender, D. Durand, & T. H. Handley (San Francisco, CA: ASP), **228**
 Bessell, M. S. 1990, *PASP*, **102**, 1181
 Breeveld, A. A., Curran, P. A., Hoversten, E. A., et al. 2010, *MNRAS*, **406**, 1687
 Brown, T. M., Baliber, N., Bianco, F. B., et al. 2013, *PASP*, **125**, 1031
 Cao, Y., Nugent, P. E., & Kasliwal, M. M. 2016, *PASP*, **128**, 114502
 Cardelli, J. A., Clayton, G. C., & Mathis, J. S. 1989, *ApJ*, **345**, 245
 Cenko, S. B., Fox, D. B., Moon, D.-S., et al. 2006, *PASP*, **118**, 1396
 Chatzopoulos, E., Wheeler, J. C., & Vinko, J. 2012, *ApJ*, **746**, 121
 Chen, T.-W., Smartt, S. J., Jerkstrand, A., et al. 2015, *MNRAS*, **452**, 1567
 Chen, T.-W., Smartt, S. J., Yates, R. M., et al. 2017, *MNRAS*, **470**, 3566
 Chevalier, R. A., & Fransson, C. 1994, *ApJ*, **420**, 268
 Chevalier, R. A., & Irwin, C. M. 2011, *ApJL*, **729**, L6
 Chugai, N. N., & Danziger, I. J. 1994, *MNRAS*, **268**, 173
 Cikota, A., De Cia, A., Schulze, S., et al. 2017, *MNRAS*, **469**, 4705
 Cooke, J., Sullivan, M., Gal-Yam, A., et al. 2012, *Natur*, **491**, 228
 Corsi, A., Gal-Yam, A., Kulkarni, S. R., et al. 2016, *ApJ*, **830**, 42
 Curtin, C., Cooke, J., Moriya, T. J., et al. 2018, *ApJ*, submitted (arXiv:1801.08241)
 Dessart, L., & Hillier, D. J. 2011, *MNRAS*, **410**, 1739
 Dessart, L., Hillier, D. J., Waldman, R., Livne, E., & Blondin, S. 2012, *MNRAS*, **426**, L76
 Dessart, L., Hillier, D. J., Yoon, S.-C., Waldman, R., & Livne, E. 2017, *A&A*, **603**, A51
 Dimitriadis, G., Sullivan, M., Kerzendorf, W., et al. 2017, *MNRAS*, **468**, 3798
 Firth, R. E., Sullivan, M., Gal-Yam, A., et al. 2015, *MNRAS*, **446**, 3895
 Fransson, C., & Kozma, C. 2002, *NewAR*, **46**, 487
 Fukugita, M., Ichikawa, T., Gunn, J. E., et al. 1996, *AJ*, **111**, 1748
 Gal-Yam, A. 2012, *Sci*, **337**, 927
 Gal-Yam, A., Kasliwal, M. M., Arcavi, I., et al. 2011, *ApJ*, **736**, 159
 Gal-Yam, A., Mazzali, P., Ofek, E. O., et al. 2009, *Natur*, **462**, 624
 Gal-Yam, A., Moon, D.-S., Fox, D. B., et al. 2004, *ApJL*, **609**, L59
 Gal-Yam, A., Nakar, E., Ofek, E. O., et al. 2008, *ApJ*, **686**, 408
 Gehrels, N., Chincarini, G., Giommi, P., et al. 2004, *ApJ*, **611**, 1005
 Heger, A., & Woosley, S. E. 2002, *ApJ*, **567**, 532
 Henden, A. A., Welch, D. L., Terrell, D., & Levine, S. E. 2009, in AAS Meeting, **214**, 407.02
 Hogg, D. W. 1999, arXiv:astro-ph/9905116
 Hogg, D. W., Baldry, I. K., Blanton, M. R., & Eisenstein, D. J. 2002, arXiv: astro-ph/0210394
 Hogg, D. W., Blanton, M., Lang, D., Mierle, K., & Roweis, S. 2008, in ASP Conf. Ser. 394, Astronomical Data Analysis Software and Systems XVII, ed. R. W. Argyle, P. S. Bunclark, & J. R. Lewis (San Francisco, CA: ASP), **27**
 Inserra, C., Nicholl, M., Chen, T.-W., et al. 2017, *MNRAS*, **468**, 4642
 Inserra, C., & Smartt, S. J. 2014, *ApJ*, **796**, 87
 Inserra, C., Smartt, S. J., Gall, E. E. E., et al. 2018, *MNRAS*, **475**, 1046
 Inserra, C., Smartt, S. J., Jerkstrand, A., et al. 2013, *ApJ*, **770**, 128
 Jeffery, D. J. 1999, arXiv:astro-ph/9907015
 Jerkstrand, A., Smartt, S. J., Inserra, C., et al. 2017, *ApJ*, **835**, 13
 Jones, D. O., Rodney, S. A., Riess, A. G., et al. 2013, *ApJ*, **768**, 166
 Junde, H., Su, H., & Dong, Y. 2011, *NDS*, **112**, 1513
 Kaiser, N., Burgett, W., Chambers, K., et al. 2010, *Proc. SPIE*, **7733**, 77330E
 Kasen, D., & Bildsten, L. 2010, *ApJ*, **717**, 245
 Kozyreva, A., & Blinnikov, S. 2015, *MNRAS*, **454**, 4357
 Laher, R. R., Surace, J., Grillmair, C. J., et al. 2014, *PASP*, **126**, 674
 Law, N. M., Kulkarni, S. R., Dekany, R. G., et al. 2009, *PASP*, **121**, 1395
 Leloudas, G., Chatzopoulos, E., Dilday, B., et al. 2012, *A&A*, **541**, A129
 Leloudas, G., Schulze, S., Krühler, T., et al. 2015, *MNRAS*, **449**, 917
 Liu, L.-D., Wang, L.-J., Wang, S.-Q., & Dai, Z.-G. 2017, arXiv:1706.01783
 Lunnan, R., Chornock, R., Berger, E., et al. 2015, *ApJ*, **804**, 90
 Lunnan, R., Chornock, R., Berger, E., et al. 2016, *ApJ*, **831**, 144
 Lunnan, R., Chornock, R., Berger, E., et al. 2018, *ApJ*, **852**, 81
 Maeda, K., Mazzali, P. A., & Nomoto, K. 2006, *ApJ*, **645**, 1331
 Maeda, K., Nakamura, T., Nomoto, K., et al. 2002, *ApJ*, **565**, 405
 Maguire, K., Sullivan, M., Pan, Y.-C., et al. 2014, *MNRAS*, **444**, 3258
 Mazzali, P. A., Nomoto, K., Patat, F., & Maeda, K. 2001, *ApJ*, **559**, 1047
 Mazzali, P. A., Sullivan, M., Pian, E., Greiner, J., & Kann, D. A. 2016, *MNRAS*, **458**, 3455
 McCrum, M., Smartt, S. J., Rest, A., et al. 2015, *MNRAS*, **448**, 1206
 Moriya, T. J., Chen, T.-W., & Langer, N. 2017, *ApJ*, **835**, 177
 Moriya, T. J., Tanaka, M., Yasuda, N., et al. 2018, *ApJ*, submitted (arXiv:1801.08240)
 Moriya, T. J., & Tominaga, N. 2012, *ApJ*, **747**, 118
 Nadyozhin, D. K. 1994, *ApJS*, **92**, 527
 Nakar, E., & Sari, R. 2010, *ApJ*, **725**, 904
 Neill, J. D., Sullivan, M., Gal-Yam, A., et al. 2011, *ApJ*, **727**, 15
 Nicholl, M., Berger, E., Smartt, S. J., et al. 2016, *ApJ*, **826**, 39
 Nicholl, M., Guillotin-Scerbonico, J., & Berger, E. 2017, *ApJ*, **850**, 55
 Nicholl, M., & Smartt, S. J. 2016, *MNRAS*, **457**, L79
 Nicholl, M., Smartt, S. J., Jerkstrand, A., et al. 2013, *Natur*, **502**, 346
 Nicholl, M., Smartt, S. J., Jerkstrand, A., et al. 2015a, *ApJL*, **807**, L18
 Nicholl, M., Smartt, S. J., Jerkstrand, A., et al. 2015b, *MNRAS*, **452**, 3869
 O'Donnell, J. E. 1994, *ApJ*, **422**, 158
 Ofek, E. O., Arcavi, I., Tal, D., et al. 2014a, *ApJ*, **788**, 154
 Ofek, E. O., Cameron, P. B., Kasliwal, M. M., et al. 2007, *ApJL*, **659**, L13
 Ofek, E. O., Fox, D., Cenko, S. B., et al. 2013, *ApJ*, **763**, 42
 Ofek, E. O., Laher, R., Surace, J., et al. 2012, *PASP*, **124**, 854
 Ofek, E. O., Zoglauer, A., Boggs, S. E., et al. 2014b, *ApJ*, **781**, 42
 Pastorello, A., Smartt, S. J., Botticella, M. T., et al. 2010, *ApJL*, **724**, L16
 Perley, D. A., Quimby, R. M., Yan, L., et al. 2016, *ApJ*, **830**, 13
 Piro, A. L. 2015, *ApJL*, **808**, L51
 Poole, T. S., Breeveld, A. A., Page, M. J., et al. 2008, *MNRAS*, **383**, 627
 Prentice, S. J., Mazzali, P. A., Pian, E., et al. 2016, *MNRAS*, **458**, 2973
 Pun, C. S. J., Kirshner, R. P., Sonneborn, G., et al. 1995, *ApJS*, **99**, 223
 Quimby, R. M., Aldering, G., Wheeler, J. C., et al. 2007, *ApJL*, **668**, L99
 Quimby, R. M., De Cia, A., Gal-Yam, A., et al. 2018, *ApJ*, **855**, 2
 Quimby, R. M., Kulkarni, S. R., Kasliwal, M. M., et al. 2011, *Natur*, **474**, 487
 Rabinak, I., & Waxman, E. 2011, *ApJ*, **728**, 63
 Rahmer, G., Smith, R., Velur, V., et al. 2008, *Proc. SPIE*, **7014**, 70144Y
 Rau, A., Kulkarni, S. R., Law, N. M., et al. 2009, *PASP*, **121**, 1334
 Roming, P. W. A., Kennedy, T. E., Mason, K. O., et al. 2005, *SSRv*, **120**, 95
 Rubin, A., Gal-Yam, A., De Cia, A., et al. 2016, *ApJ*, **820**, 33
 Schlafly, E. F., & Finkbeiner, D. P. 2011, *ApJ*, **737**, 103
 Schulze, S., Krühler, T., Leloudas, G., et al. 2018, *MNRAS*, **473**, 1258
 Scovacricchi, D., Nichol, R. C., Bacon, D., Sullivan, M., & Prajs, S. 2016, *MNRAS*, **456**, 1700
 SDSS Collaboration, Albareti, F. D., Allende Prieto, C., et al. 2017, *ApJS*, **233**, 25
 Seitenzahl, I. R., Timmes, F. X., & Magkotsios, G. 2014, *ApJ*, **792**, 10
 Smith, M., Sullivan, M., D'Andrea, C. B., et al. 2016, *ApJL*, **818**, L8
 Smith, N., Li, W., Foley, R. J., et al. 2007, *ApJ*, **666**, 1116

- Steele, I. A., Smith, R. J., Rees, P. C., et al. 2004, *Proc. SPIE*, **5489**, 679
- Stritzinger, M., & Leibundgut, B. 2005, *A&A*, **431**, 423
- Sullivan, M., Howell, D. A., Perrett, K., et al. 2006, *AJ*, **131**, 960
- Taddia, F., Sollerman, J., Fremling, C., et al. 2018a, *A&A*, **609**, A106
- Taddia, F., Sollerman, J., Leloudas, G., et al. 2015, *A&A*, **574**, A60
- Taddia, F., Stritzinger, M. D., Bersten, M., et al. 2018b, *A&A*, **609**, A136
- Thöne, C. C., de Ugarte Postigo, A., García-Benito, R., et al. 2015, *MNRAS*, **451**, L65
- Thuan, T. X., & Gunn, J. E. 1976, *PASP*, **88**, 543
- Tody, D. 1986, *Proc. SPIE*, **627**, 733
- Tody, D. 1993, in ASP Conf. Ser. 52, Astronomical Data Analysis Software and Systems II, ed. R. J. Hanisch, R. J. V. Brissenden, & J. Barnes (San Francisco, CA: ASP), 173
- Valenti, S., Howell, D. A., Stritzinger, M. D., et al. 2016, *MNRAS*, **459**, 3939
- Valenti, S., Taubenberger, S., Pastorello, A., et al. 2012, *ApJL*, **749**, L28
- van Dokkum, P. G. 2001, *PASP*, **113**, 1420
- Vreeswijk, P. M., Leloudas, G., Gal-Yam, A., et al. 2017, *ApJ*, **835**, 58
- Vreeswijk, P. M., Savaglio, S., Gal-Yam, A., et al. 2014, *ApJ*, **797**, 24
- Wheeler, J. C., & Benetti, S. 2000, in Allen's Astrophysical Quantities, ed. A. N. Cox (4th ed.; New York: Springer), 451
- Williams, M. J., Bureau, M., & Cappellari, M. 2010, *MNRAS*, **409**, 1330
- Woosley, S. E. 2010, *ApJL*, **719**, L204
- Yan, L., Lunnan, R., Perley, D., et al. 2017, *ApJ*, **848**, 6
- Yan, L., Quimby, R., Ofek, E., et al. 2015, *ApJ*, **814**, 108
- York, D. G., Adelman, J., Anderson, J. E., Jr., et al. 2000, *AJ*, **120**, 1579
- Zacharias, N., Monet, D. G., Levine, S. E., et al. 2004, *BAAS*, **36**, 1418